USING NUMERICAL SIMULATIONS TO ASSESS URBAN HEAT ISLAND MITIGATION BY CONVERTING VACANT AREAS INTO GREEN SPACES

By

Timothy John Cady

Submitted to the graduate degree program in Department of Geography & Atmospheric Science and the Graduate Faculty of the University of Kansas in partial fulfillment of the requirements for the degree of Master of Science.

Dr. David Rahn, Chairperson

Committee members

Dr. Nathaniel Brunsell

Dr. Ward Lyles

Date defended: 19 November 2019

The Thesis Committee for Timothy John Cady certifies
that this is the approved version of the following thesis :

USING NUMERICAL SIMULATIONS TO ASSESS URBAN HEAT ISLAND MITIGATION BY CONVERTING VACANT AREAS INTO GREEN SPACES

Dr. David Rahn, Chairperson

Date approved: 19 November 2019

Abstract

Impervious surfaces and buildings in the urban environment alter the radiative balance and energy exchange in the boundary layer, increasing sensible heat flux and decreasing latent heat flux near the surface. This typically results in a positive temperature anomaly known as the urban heat island (UHI). The UHI has been attributed to increases in heat related-illness and mortality. Continued urbanization and anthropogenic warming will enhance the magnitude of UHIs worldwide in the coming decades, raising the need for viable mitigation strategies. Observational studies indicate that green spaces within urban areas can reduce local surface temperature by increasing evaporative cooling and latent heat flux, suggesting that implementing such spaces on a widespread scale may be a viable option to lessen the impacts of the UHI. This work explores the potential impact on the UHI if existing vacant lots are converted to green spaces.

The Weather Research and Forecasting (WRF) model was used to simulate the Kansas City, MO region with an inner domain grid spacing of 300 m that allows for block-level analysis. Within WRF, the Single Layer Urban Canopy Model (SLUCM) accounts for the combined radiative effects of natural land cover, vegetation, impervious cover, and building surfaces. Three simulations of summertime heat wave events between 2011 and 2013 are investigated, and model output was validated with surface observations. Using vacant property data and identifying places with a high fraction of impervious surfaces, the most suitable "focus area" for converting vacant lots to green spaces was determined. WRF geographic datasets were modified to simulate varying degrees of realistic conversion of urban to green spaces in these areas. The three control cases

under each greening strategy were repeated with the modified geographic datasets, and the local cooling effect using each strategy was compared to each initial control run. Results show that under more aggressive greening strategies, a mean local cooling impact of 0.5 to 1.0 °C was present within the focus area itself during the nighttime hours following the development of the stable nocturnal boundary layer. Furthermore, additional cooling via the "park cool island" is of up to 1.0 °C possible up to 1 km downwind of the implemented green spaces. Quantifying the thermal impact of converting vacant lots with impervious surfaces to green spaces is an additional factor that can be taken into consideration by policy makers when considering the abatement of the UHI. It is hoped that the focus of this study will serve as guidance to both planners and atmospheric scientists alike as part of the effort to promote future sustainable cities.

Acknowledgements

Well, it's been quite the ride. I first and foremost would like to thank my advisor, Dr. David Rahn, for his continued guidance and constant willingness to help through the duration of my time at KU, even after I moved 1,000 miles away to chase my dream career. I would also like to thank my committee members, Dr. Ward Lyles and Dr. Nathaniel Brunsell for their helpful input and perspectives on topics to which I had not been previously exposed. I of course also owe my thanks to the faculty and staff of the Department of Geography and Atmospheric Science and of course to the "Lindley Late Night Squad" for making my time in graduate school and enjoyable and enriching one despite all the long nights which on occasion became early mornings.

I would have never been able to reach this goal without the unwavering support of my family, who have always encouraged me to follow my dreams since I was a young kid with a mind set on a goal. For that, I owe you a lifetime of gratitude. I furthermore owe countless thanks to the great people that I have had the pleasure of getting to know in Lawrence throughout the past 2 and a half years. To the Gribblers, for helping me reach new heights I never thought I could reach, the KC Kop, for all the mornings at the Dubliner and our excursion to Ann Arbor, and to many, many others: I deeply thank you all for the friendship, support, and lifelong memories. *It's the wonder of nature, baby!!*

"*Only the disciplined ones are free in life. If you are undisciplined, you are a slave to your moods. You are a slave to your passions.*"

– Eliud Kipchoge

Contents

List of Figures

List of Tables

Chapter 1

Introduction

1.1 The Urban Heat Island

Humanity is currently in the midst of a period of rapid and sustained urbanization. Since 1950, the proportion of the world's population living in cities has risen sharply from approximately 30% to over 54% (United Nations 2015). This number is likely to eclipse-two thirds by 2050, accompanied by the addition of 2.5 billion new residents to the world's cities and an expansion of global urban land area by up to 1.5 million km^2 (Seto *et al.* 2014). A consequence of this demographic shift is the disruption of local climate systems due to changes in land use. Urbanization is characterized by the replacement of natural land cover with low-albedo impervious surfaces such as roads and buildings. Replacing vegetation with urban surfaces alters the local surface radiative balance and energy exchange, reducing evapotranspiration, and thus reducing latent heat flux and increasing sensible heat flux (Oke 1988; Taha 1997; Arnfield 2003). Consequently, cities tend to exhibit positive land surface temperature (e.g. Tran *et al.* 2006; Imhoff *et al.* 2010; Peng *et al.* 2011) and air temperature anomalies (e.g. Oke 1995; Azevedo *et al.* 2016) when compared to their rural surroundings, a phenomenon known as the urban heat island (UHI) (Oke 1982). This effect can be further exacerbated by the three-dimensional morphology of a city's buildings and roads, which form an "urban canyon" that traps outgoing longwave radiation within the planetary boundary layer (PBL) and has a greater capacity to store heat in building wall and roof surfaces (Nunez & Oke 1977; Ryu & Baik 2012). UHIs are magnified by anthropogenic processes, most notably from the use of air conditioning systems and emissions from vehicles and industrial activity (Shahmohamadi *et al.* 2011; Salamanca *et al.* 2014).

As both urbanization and anthropogenic global warming become increasingly prevalent over the next several decades and present numerous threats to overall human sustainability, it is crucial to consider land use decisions that have the potential to mitigate the impacts of the UHI. A possibly effective avenue to counter its effects is urban greening, which involves the replacement of some existing urban surfaces with green spaces such as small parks and forests (Schilling & Logan 2008). Such a plan may prove to be particularly viable in urban areas with high amounts of vacant structures and unused impervious surfaces, which could be converted without causing any displacement of the area's residents. While urban greening is economically infeasible to test on a widespread scale, the development of high-resolution mesoscale weather models in recent years allows for a detailed numerical simulation of the UHI and its response to various changes to land use (Chen *et al.* 2011). *The goal of this project is to utilize numerical model simulations to determine the utility of urban greening through a realistic land use conversion based on current locations of abandoned property as a viable and realistic strategy to mitigate UHIs.* In doing so, we hope to guide future urban land use decisions by demonstrating how such a strategy could lessen the impact of extreme heat in urban areas.

UHI intensity (UHII) is defined as the difference in observed temperature between characteristic urban and rural locations (Memon *et al.* 2009), and has been observed as high as 12°C (Tran *et al.* 2006). Quantifying UHII is further complicated by the fact that UHIs manifest both at the surface and across multiple layers of the atmosphere, and therefore are defined using varying strategies (Oke 1995). The surface UHI (SUHI) is diagnosed by analyzing the distribution of satellite-derived land surface temperature (LST) across an area and its relation to indicators of urbanization such as normalized difference vegetation index (NDVI), impervious surface area (ISA), and urban fraction (e.g. Yuan & Bauer 2007; Li *et al.* 2011; Hu & Brunsell 2015). While the analysis of SUHIs is useful in that satellite-based datasets provide widespread areal coverage of urban areas, using these products to examine the diurnal evolution of UHIs is ultimately limited by low temporal resolution and potential issues associated with the use of atmospheric correction algorithms to derive temperature (Voogt & Oke 2003). Conversely, air temperature observations

detect atmospheric heat islands within both the urban canopy layer (i.e. the layer of the atmosphere below the mean building height) and the PBL (e.g. Childs & Raman 2005; Zhou & Shepherd 2010; Barlow *et al.* 2015). Atmospheric UHII tends to be strongest in the evening hours (Oke 1988) and under weak anticyclonic synoptic flow regimes (Hardin *et al.* 2017), often reducing or eliminating stable stratification within nocturnal boundary layer (Mahrt 1998). Although ground-based observations of these features are more sparse in coverage, they offer both a direct measure of temperature and higher temporal resolution compared to their satellite-based counterparts (Voogt 2007). This allows for a more detailed analysis of UHI behavior over time, albeit with limited capabilities to examine the spatial structure.

UHIs are particularly severe during heat wave events, broadly defined as multi-day periods where both the daytime high and nighttime low temperatures exceed a defined climatological threshold (Robinson 2001). Such events are the most frequent weather-related cause of death in the United States since 1970 (Borden & Cutter 2008). It has been well established that the anticipated future impacts of anthropogenic climate change are expected to increase both the frequency and magnitude of heat wave events in the coming years, thus increasing the risks associated with them in urban areas (Meehl & Tebaldi 2004; Field 2017). During heat waves, surface moisture availability in urban areas is limited, which further reduces evapotranspiration rates and enhances UHII (Li & Bou-Zeid 2013; Zhao *et al.* 2018). This impact is compounded by the increased energy demand associated with the higher usage rates of indoor cooling systems, which increases anthropogenic heating and creates a feedback loop of higher temperatures driving greater energy consumption (Revi *et al.* 2014; Salamanca *et al.* 2014). Consequently, residents of cities are impacted by heat stress for prolonged periods due to the combined synergistic effects of the UHI and heat waves, a prospect which has severely negative ramifications for public health and human sustainability (Tan *et al.* 2010). Incidences of extreme heat in urban areas have been attributed to a myriad of serious health problems that are further worsened by the effects of the UHI, particularly increased rates of fatigue, heat exhaustion, renal failure via heat stroke, and respiratory sicknesses due to increased ozone production (Frumkin 2002). Furthermore, anomalously warm temperatures in urban areas

have been associated with statistically significant increases in weekly suicide rates, suggesting that these impacts may also manifest in both physical and mental health (Dixon *et al.* 2014). These issues arise not only from the UHI enhancement of elevated high temperatures, but also due to its elevation of nocturnal lows which effectively prevent the human body's recovery from heat stress experienced during the daytime hours (Murage *et al.* 2017). Given the numerous health impacts of the UHI, it is perhaps also unsurprising that a relationship between elevated heat-related mortality in cities and UHI impacts has been widely identified, particularly among the impoverished and other vulnerable socioeconomic groups that may lack access to cooling resources needed to prevent heat-related illnesses (Johnson & Wilson 2009). This harsh reality is reflected in the impacts of major heat wave events in recent decades, such as the 1995 event which caused over 700 deaths in Chicago and the 2003 event deemed responsible for over 15,000 deaths in continental Europe (Semenza *et al.* 1996; Fouillet *et al.* 2006).

1.2 UHI and Urban Greening

With the identified present and future risks to urban populations posed by UHIs, an array of potential strategies have been explored to mitigate their impacts as both anthropogenic warming and widespread urbanization progress throughout the coming decades (Akbari *et al.* 2016). These can essentially be separated into two main categories: the modification of surface and building materials, and the incorporation of green-spaces and vegetation into the urban core.

Altering the thermal properties and absorptivity of impervious urban surfaces and building materials can diminish UHII without making drastic changes to land use. Surface-based mitigation strategies involve increasing the reflectively of pavement and asphalt by adding specialized materials in production, using reflective paints and sealants to increase albedo, and implementing color changing surfaces that adapt to the diurnal radiation cycle (Takebayashi & Moriyama 2007; Susca *et al.* 2011). Furthermore, increasing the permeability of surface materials can increase moisture availability and thus evapotranspiration rates (Santamouris 2013). Efforts to reduce UHII through the alteration of building materials are generally centered around modifying roof cover. "Green

roofs", where roof surfaces are replaced with vegetation, act to increase surface albedo, increase latent heat flux, and enhance evapotransporative processes within the urban boundary layer (Santamouris 2014). A second approach involves the implementation of reflective materials to building roofs, which increases albedo and reduce sensible heat flux much like at street level (Takebayashi & Moriyama 2007; Santamouris 2013).

While UHI mitigation benefits associated with changes to materials are documented, the preservation and incorporation of open space and natural vegetation among the built environment also offers the potential to drastically reduce the effects of the UHI (Hart & Sailor 2009). Modifying existing surface cover (i.e. the replacement of impervious surfaces with natural cover and vegetation) is an effective way to reduce air temperatures within the urban canopy layer, but also is a more intrusive UHI mitigation option option. Many observational studies (e.g. Oliveira *et al.* 2011; Declet-Barreto *et al.* 2013; Feyisa *et al.* 2014) have demonstrated a significant "park cool island" effect associated with urban green spaces of varying sizes and configurations, with cooling impacts often extending into non-vegetated areas. The addition of green spaces such as parks, crops, and urban forests into an existing city landscape is an unrealistic UHI mitigation option for highly developed and high density areas. However, a strong opportunity for UHI reduction lies specifically within the "greening" of vacant or unused impervious surfaces and buildings, a strategy that could prove particularly useful in cities that have experienced significant recent declines in population and thus contain high amounts of vacant space. Beyond the impact of UHII reduction, doing so also has the potential to increase property values in economically depressed areas while offering residents of these areas the chance to become engaged in the planning process (Schilling & Logan 2008; Heckert & Mennis 2012). These benefits are exemplified by cities like Detroit, which has undertaken a widespread effort to promote the incorporation of green infrastructure and urban farming into redevelopment plans, particularly in areas with widespread swaths of vacant land (Colasanti *et al.* 2012; Meerow & Newell 2017). While the exact effects of greening vacant and unused urban spaces is difficult to quantify on a large scale, the strategy's potential positive impacts suggest that it should be explored further as a means of combating the anticipated future

threats posed by UHIs and anthropogenic global warming.

1.3 Motivation and Objectives

Recent advances in computational capabilities permit the UHI and its response to changes in land cover, building properties, and surface materials to be simulated with high-resolution numerical weather models, allowing for the thermal impacts of urban greening to be examined in greater detail. This is possible due to the development of advanced urban parameterization schemes and data assimilation techniques that are incorporated within models such as the Weather Research and Forecasting (WRF) model, a numerical weather prediction system capable of simulating atmospheric processes at a variety of scales (Skamarock *et al.* 2005). Additionally, the availability of high-resolution land use/land cover (LULC) data has allowed for surface properties to be realistically represented. Within the WRF system, the coupling of urban canopy models (UCM) to the unified Noah Land Surface Model (LSM) allow for UHIs to be resolved at fine scales. UCMs of varying complexities have been implemented into the WRF system, ranging from a simplified bulk parameterization to complex multilayer canopy models which take into account detailed urban morphology characteristics, building material parameters, and anthropogenic heat release (Chen *et al.* 2011).

Although high resolution UHI modeling in WRF is computationally expensive and thus not viable for operational implementation, it is a useful tool for assessing the potential impact of changes to the urban environment on aggravating or mitigating UHII. Previous research has been largely focused on modifying surface material, building properties, and anthropogenic emissions in the existing urban environment to assess the utility of UHI mitigation strategies (e.g. Morini *et al.* 2016; Salamanca *et al.* 2012; Zhou & Shepherd 2010). Given the aforementioned cooling benefits of urban greening, however, it is necessary to evaluate strategies that can be implemented to combat the UHI in urban areas, particularly by implementing new green spaces into these areas. Studies of this particular subject have been rather limited despite the large societal implications of future urbanization and climate change. Some recent studies (e.g. Fu & Weng 2017; Giannaros *et al.*

2018) have implemented WRF to simulate the response of the UHI to potential future land use and greening scenarios. However, additional simulations across a diverse set of locations are needed to quantify the impact of planning and land use strategies on worldwide UHII mitigation.

This project seeks to bridge physical science and urban planning by examining model simulations of the UHI that reflect the conversion of vacant land and abandoned properties to green spaces. We use WRF with the Noah LSM coupled to the SLUCM to simulate the thermal effects of converting vacant areas to green spaces during heat wave events. The area of focus is the Kansas City metropolitan area, a mid-sized temperate North American city experiences frequent heat wave events and contains areas with high amounts of vacant space. Using high resolution LULC data from the National Land Cover Database's 2011 product and vacancy data from the 2010 United States Census, we identify an area with potential for widespread urban greening. After assimilating the land use data into WRF, it is subsequently modified to reflect various magnitudes of urban greening within the identified area. Three heat wave cases are simulated using WRF with varied levels of implemented greening. Model output is analyzed for each heat wave case and each greening level to assess the impacts of urban greening on air temperature, both within and surrounding the modified area to examine the local and non-local impacts. The overall goal is to quantify the effects of the different levels of greening on the UHI, and assess if the conversion of vacant areas within cities offers enough of a benefit to be a viable planning strategy for future consideration. While the conclusions of this study will not present any specific planning recommendations, the results presented here can be utilized by policy stakeholders to contribute towards effective and equitable solutions to the growing challenge of heat island mitigation.

Chapter 2

Experimental Design and Model Validation

2.1 Study Area

The Kansas City Metropolitan Statistical Area consists of 14 counties along the northern Kansas-Missouri border with a combined population of approximately 2.13 million (U.S. Census Bureau 2018). The Mid-America Regional Council (MARC) oversees regional planning for nine counties and 119 cities within the region, which is the area of focus for this study (MARC 2018). The region exhibits a widespread LULC diversity which makes it an ideal location for simulating the structure and evolution of the UHI, encompassing the densely populated urban center of Kansas City (pop. 488,943), surrounding areas of urban sprawl and suburban development, and expansive peripheral areas of cropland, forests, and pastures (Figure 2.1). Kansas City and its surroundings have experienced robust growth in recent years, increasing in population by approximately 16% since 2000 (U.S. Census Bureau 2011). Furthermore, the area's mid-latitude inland location has made it prone to prolonged, synoptically-driven heat waves in the past, most notably including an event in 1980 that was responsible for a 65% increase in mortality (Jones *et al.* 1982).

Examining the urban core of Kansas City in detail reveals its status as a strong candidate for large-scale urban greening to counter the current and expected future impacts of the UHI. Like many other locations across the central United States, the city has suffered from high rates of vacant land and abandoned buildings brought on by the combined forces of population loss, economic disinvestment, and racial segregation during the mid-20th century (Pagano & Bowman 2000; L'Heureux 2015). A review of data from the 2010 U.S. Census shows that high vacancy rates persist across portions of the Kansas City despite recent revitalization efforts, particularly in

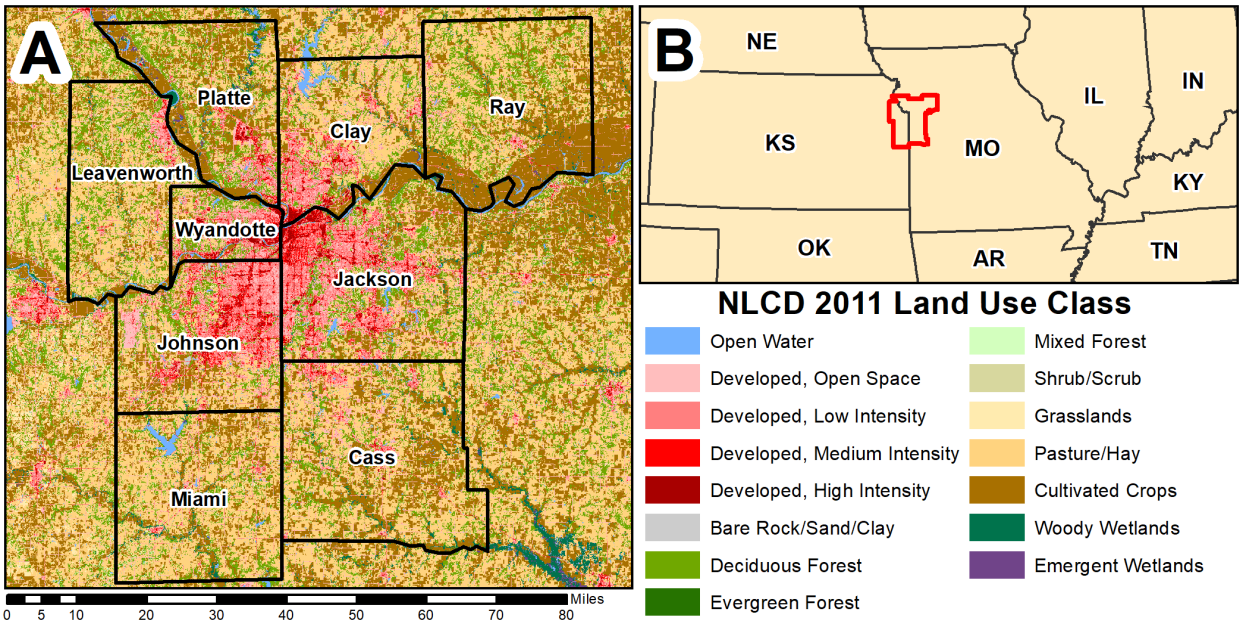

Figure 2.1: Overview of the study area: (A) Land use classification (shaded) from the 2011 National Land Cover Database for the nine counties (black outline) of the MARC region; (B) Location of the study area (red outline) within the central United States.

its southeastern portion along the corridor to the east of Troost Avenue (Figure 2.2A). The Troost Avenue corridor, described as "...one of the primary symbols in Kansas City of disinvestment and racial and economic segregation from the 1950's to today", has lower socioeconomic status and diminished property values compared to surrounding portions of the metropolitan region (MARC 2013). Historical disinvestment further manifests itself throughout the area through public health inequities, which has been identified as a hot-spot for elevated asthma-related hospital visits, low birth weights, and decreased overall life expectancy (City of Kansas City 2017).

Using block-level data from the 2010 U.S. Census, a region consisting of mostly single-family residential neighborhoods (MARC 2013) and encompassing and extending eastward from the Troost Avenue corridor could potentially be well-suited for large-scale LULC conversion (Figure 2.2B). Within the chosen area, 5,589 out of a total of 19,893 residential units were classified as vacant, giving an overall rate of approximately 28%. Considering the greater region's history and high rate of vacant structures, the implementation of widespread urban greening within this focus area has the potential to reduce ambient temperatures during heat wave events while also

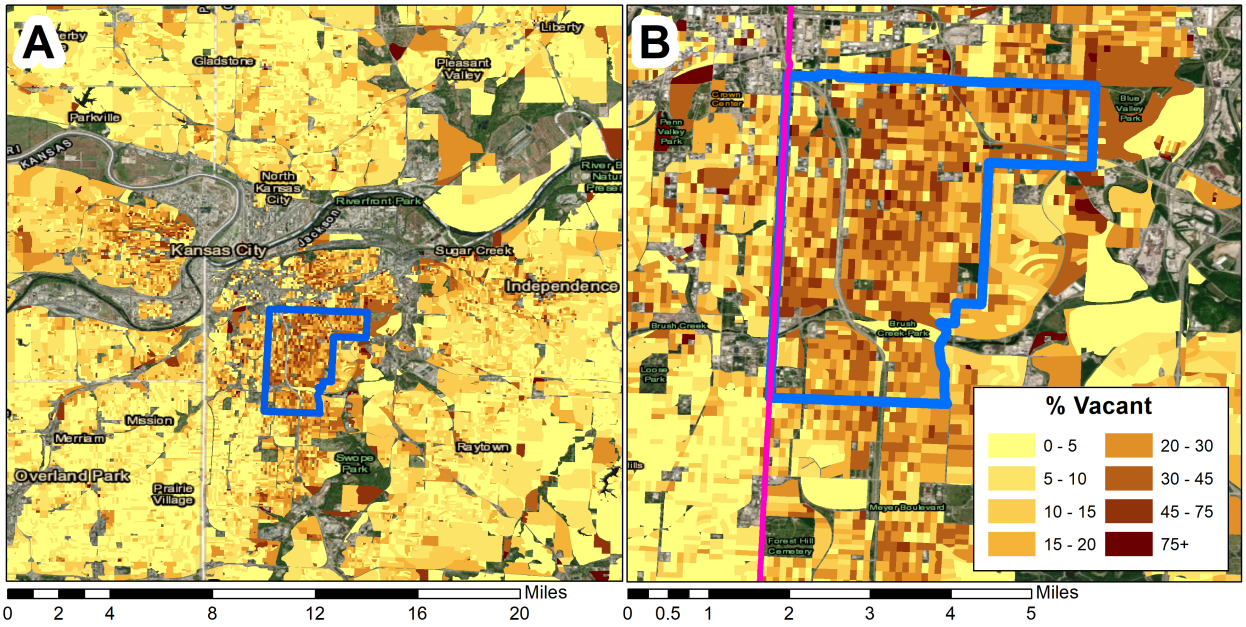

Figure 2.2: Block-level overall vacancy rates (shaded, percent) derived from the 2010 U.S. Census with the chosen greening area highlighted (blue) for (A) the greater Kansas City region and (B) the focus area itself, with Troost Avenue highlighted (pink).

addressing the unequal structural systems that have shaped its development in the past.

2.2 Description of the Model System

The Advanced Research Weather Research and Forecasting Model (WRF-ARW) is a fully compressible, non-hydrostatic numerical weather model (Skamarock *et al.* 2005). WRF (version 4.0.1) is used to examine urban greening strategies for cooling the selected region during periods of extreme heat and thereby reduce the local CLUHI. The ability of WRF simulations to represent the behavior of UHIs at fine scales is thoroughly documented (Chen *et al.* 2011), and the model has been widely utilized to examine the mesoscale response of urban temperatures to changes in LULC and variations in anthropogenic activity (e.g. Li & Norford 2016; Fu & Weng 2017; Giannaros *et al.* 2018).

In a similar manner to previous UHI modeling efforts (e.g. Salamanca *et al.* 2012; Gutiérrez *et al.* 2015), a two-way nested horizontal grid setup is used to reduce computational expense while still capturing the area of interest at sufficient resolution. The full extent of the model domain

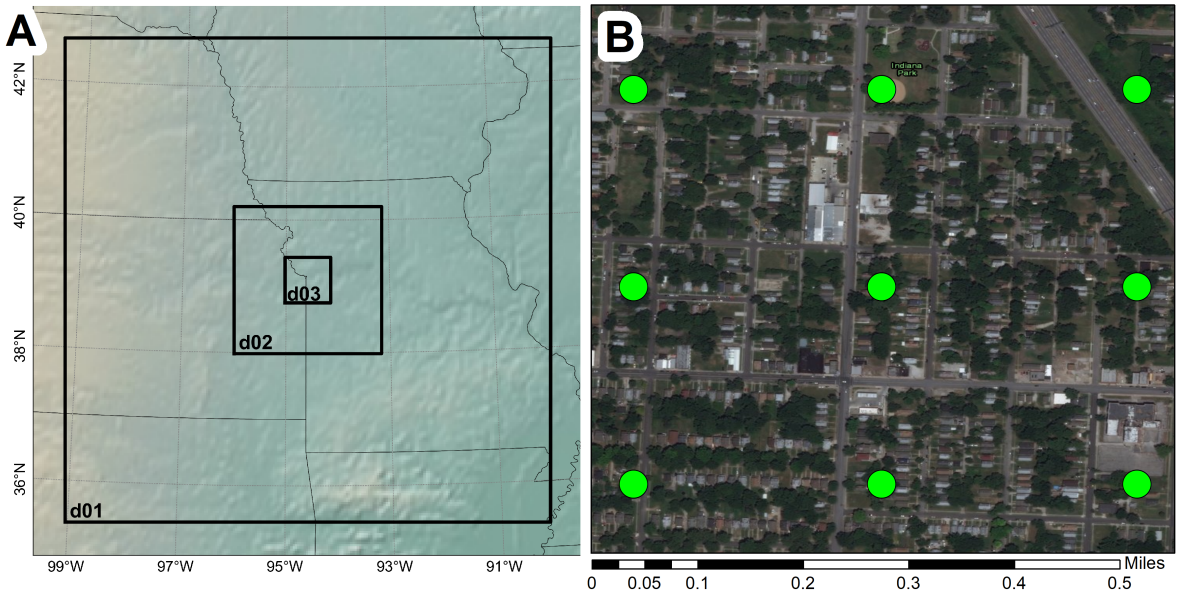

Figure 2.3: (A) Nested domain boundaries (black, labeled) used in the WRF simulations performed during this study. (B) Example of grid point locations within d03 (green circles), representing processes at approximately block-level (0.3km).

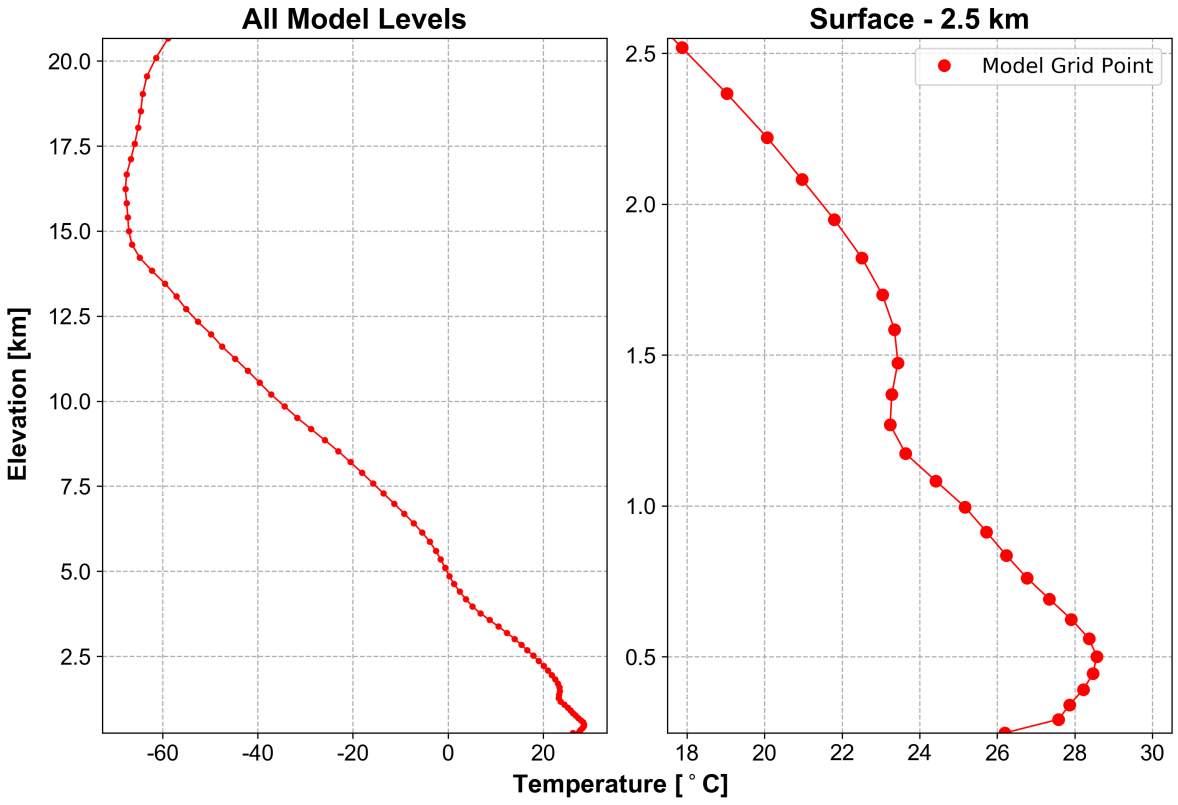

Figure 2.4: Simulated vertical temperature profile (°C) for Kansas City Downtown Airport (39.121°N, 94.590°W) at 0000 UTC 21 July 2012, with model elevation levels (km, red circles) depicted for the full vertical extent (left) and the surface to 2.5km layer (right).

covers an area of approximately 656,100 km^2, consisting of three nested grids with horizontal resolutions of 7.5 km (d01), 1.5km (d02), and 0.3km (d03) and grid sizes of 108 x 108, 164 x 164, and 254 x 254 points, respectively (Figure 2.3A). There are 82 vertical eta levels for all domains, spaced more finely near the surface to better represent temperature variation within the PBL and resolve features such as the stable nocturnal boundary layer (Figure 2.4). The innermost model domain encompasses the full extent of Kansas City at approximately block-level scale, providing greater detail than in other comparable modeling studies (Figure 2.3B). Subsequent analysis uses the output from d03.

The WRF Preprocessing System (WPS) processes meteorological and geographic datasets for interpolation to the defined model grids. All WRF simulations for this study were initialized using the National Centers for Environmental Prediction's (NCEP) North American Mesoscale Forecast System analysis (NAM-ANL) product, consisting of atmospheric variables at 42 constant pressure levels output every 6 hours at 12 km horizontal resolution. These data supply the initial and lateral boundary conditions for d01 throughout the duration of each model run. Boundary conditions for the inner two nested grids are provided by their respective parent domains, thus reducing discontinuities in spatial and temporal resolution between the fine inner WRF domains and the courser reanalysis data used to initialize the model.

Three high-resolution geographic datasets were ingested into WPS to obtain a detailed representation of land use and urban morphology characteristics across the model domain that could be modified to reflect potential future urban greening within the area of focus. LULC data were acquired from the 2011 National Land Cover Database (NLCD) Land Cover product, a 30-meter categorical land use classification derived from Landsat Thematic Mapper imagery (Homer *et al.* 2015). This is accompanied in the NLCD dataset by additional products which provide estimates of impervious surface coverage and tree canopy fraction for each grid cell. Elevation data were obtained at 30 arc-second resolution from the U.S. Geological Survey (USGS) 2010 Global Multi-Resolution Terrain Elevation dataset (Danielson & Gesch 2011). Detailed urban statistics (e.g. building height distributions, street canyon width) were obtained from the National Urban Data

and Access Portal Tool (NUDAPT) for use in the calculation of morphology parameters such as surface roughness length and sky-view factor (Glotfelty *et al.* 2013).

Given that the geographic datasets are higher resolution than the 300-m grid spacing in d03, they must be upscaled and interpolated to the model domain by WPS. The interpolation is a simple average of all source data points nearer to a particular grid point than any other grid point. More detailed variation in LULC is retained by including the distribution of raw data points within each model grid cell as an array of fractional values for each land use category (LANDUSEF). Land surface characteristics for the model grid are calculated using these arrays and an associated lookup table containing parameters for the NLCD dataset (see Appendix A). It was thus possible to capture the impact of subgridscale variability in LULC across the Kansas City area without requiring model simulations at an inordinately fine scale. Similarly, interpolated grids were also constructed from the geographic data for fractional impervious surface area (IMPERV), fractional green area (GREENFRAC), total urban fraction (FRCURB2D), tree canopy fraction (CANFRA) and the 132 urban morphology parameters obtained from the NUDAPT product (URBPARAM).

A vast array of parameterization schemes are available within WRF that represent subgrid atmospheric processes which cannot be explicitly resolved without prohibitively high computational expense (Skamarock *et al.* 2005). The chosen model physics settings for this study is in Table 2.1. Urban effects in the WRF system are primarily driven by the interaction between three key components. Surface sensible and latent heat fluxes are determined by coupling the Unified Noah Land Surface Model (LSM), which represents fluxes associated with natural land cover and vegetation, with an urban canopy model (UCM), which represents fluxes associated with the built environment (Chen *et al.* 2011). These properties are ingested by the surface layer scheme, which in turn characterizes near-surface turbulent mixing and mass transport and then the planetary boundary layer scheme. Considering the importance of these processes in the development of UHIs, the choice of these settings is a critical factor in producing simulations representative of the real atmosphere. However, no single configuration has been determined to best resolve UHIs across different locations and climates. It was therefore necessary to conduct a series of sensitivity tests to determine

the choice of physics settings most suited for simulating the Kansas City UHI before using the model to determine impacts to modified green spaces.

Table 2.1: List of parameterization schemes utilized to resolve subgrid microphysical and radiative processes within the WRF model system.

WRF Physics Configuration

Physics Option	**Parameterization**	**Reference**
Microphysics	WRF Single-Moment 3 Class	Hong *et al.* 2004
Shortwave Radiation	RRTMG	Iacono *et al.* 2008
Longwave Radiation		
Surface Layer	Eta Similarity Scheme	Janjić 1994
Cumulus (*d01 only*)	Kain–Fritsch Scheme	Kain 2004
Boundary Layer	Bougeault–Lacarrere Scheme	Bougeault & Lacarrere 1989
Land Surface	Unified Noah LSM	Tewari *et al.* 2004
Urban Physics	Single Layer Urban Canopy Model	Chen *et al.* 2011

2.3 Model System Validation

WRF includes several parameterization options of varying complexity to represent subgridscale urban effects. The simplest of these is a bulk scheme which characterizes all urban surfaces with a constant roughness length, surface albedo, heat capacity, and thermal conductivity (Chen *et al.* 2011). While this simplified approach has been successfully utilized in simulations of the UHI (e.g. Li *et al.* 2017, Liu *et al.* 2006), it is limited by its ability to capture the thermal impacts of heterogeneous urban landscapes at small scales. It is therefore not included in the evaluation of the model system for this study. UCMs, two of which have been integrated into the WRF system, represent the impacts of urban surfaces on the surface momentum and energy balance in greater detail. The single-layer urban canopy model (SLUCM) is the simpler of the two options, but it has achieved widespread use in WRF analyses of the ability of green spaces to cool urban

areas (e.g. Papangelis *et al.* 2012; Giannaros *et al.* 2018). SLUCM characterizes the urban canopy layer as a single two-dimensional column, and it includes mass and energy exchanges between the lower atmosphere and the canopy's roof, wall, and street surfaces (Kusaka *et al.* 2001). Street canyons are parameterized as infinitely long with variable orientation angles and building heights, widths, and thermal characteristics included to reflect heterogeneous urban morphology. This allows for the effects of shadows, radiation trapping, and diurnal changes in the solar azimuth angle to be considered in calculations of radiative transfer. Sensible and latent anthropogenic heat may optionally be added to the system using a constant maximum value and a lookup table of fractional heating amounts based on the local time. A more complex UCM is provided via the building effect parameterization (BEP), which characterizes the three-dimensional structure of mass and momentum transport across multiple layers of the urban canopy (Martilli *et al.* 2002). By considering the radiative effects of both horizontal and vertical building and street surfaces, BEP is able to more explicitly capture the generation of turbulent kinetic energy within the canopy and its mixing via wake diffusion. As a result, interactions between the canopy layer, roughness sublayer, and PBL are represented in greater detail than with a single-layer model (Figure 2.5). BEP is typically coupled with the building energy model (BEM), which parameterizes energy exchange between building interiors and the surrounding environment (Salamanca *et al.* 2010). BEM accounts for the effects of ventilation, building occupancy, energy consumption, and air conditioning usage, thereby providing a more comprehensive depiction of anthropogenic heating within urban canyons. Because BEP+BEM is relatively similar in structure to BEP alone, only the coupled system was utilized in sensitivity tests along with SLUCM to assess and validate the performance of WRF.

Three boundary layer parameterizations were assessed for use in the WRF simulations: the Mellor–Yamada–Janjic (MYJ) scheme (Janjić 1994), the Bougeault–Lacarrere (BouLac) scheme (Bougeault & Lacarrere 1989), and the Yonsei University (YSU) scheme (Hong *et al.* 2006). MYJ and BouLac each employ a 1.5-order local closure model, with the height of the PBL defined using a minimum turbulent kinetic energy threshold value (0.2 m^2/s^2 for MYJ and 0.005 m^2/s^2

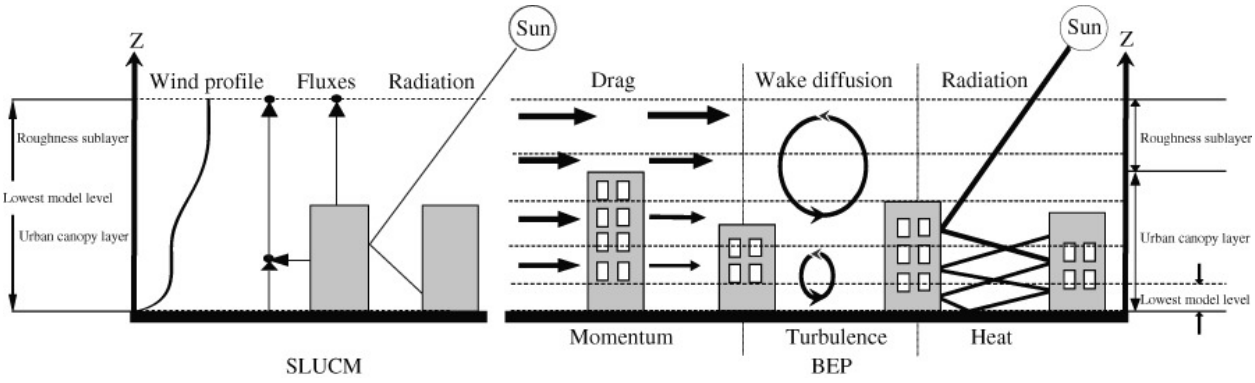

Figure 2.5: Schematic of radiative and energy transfer processes parameterized within urban areas by SLUCM (left) and BEP (right). Figure reprinted from Chen *et al.* 2011, *International Journal of Climatology* **31**, 273–288.

for MYJ). Conversely, YSU utilizes first-order non-local closure and defines the PBL height at the level where the local Bulk Richardson Number reaches 0.25 (Banks *et al.* 2016).

The 2-meter air temperature (T_{2m}) is a diagnostic variable in the coupled Noah LSM-UCM system that is calculated from the prognostic surface energy balance and LST terms as outlined in Li & Bou-Zeid 2014. For model grid cells with an urban land use classification, the relative contributions of both impervious and vegetated surfaces are considered in calculating the surface temperature:

$$LST = f_{urb} * LST_{urb} + (f_{urb} - 1) * LST_{veg} \tag{2.1}$$

where f_{urb} represents the grid cell's impervious surface fraction obtained from IMPERV and LST_{veg} is the LST calculated in Noah LSM via surface energy balance. LST_{urb}, the LST for impervious surfaces, is alternatively obtained from the UCM as follows:

$$LST_{urb} = T_a + \frac{H_{urb}}{\rho * C_h * U} \tag{2.2}$$

where T_a, ρ, and U are the prognostic air temperature, air density, and wind speed respectively at the lowest model level and C_h is the turbulent transfer coefficient over land, and H_{urb} represents the combined sensible heat fluxes of surfaces within the urban canyon. T_{2m} is derived for urban

grid cells using the following relationship:

$$T_{2m} = LST - \frac{H}{\rho * C_{h2m} * U_{2m}} \tag{2.3}$$

where LST is the surface temperature obtained in Equation 2.1, H represents the combined urban and vegetative sensible heat fluxes ($f_{urb} * H_{urb} + (f_{urb} - 1) * H_{veg}$), and ρ, C_{h2m}, and U_{2m} are the air density, turbulent transfer coefficient, and wind speed respectively at 2 meters above the surface.

To determine the physics options most acceptable for use in the experimental urban greening simulations, a 108-hour sensitivity run was performed for each possible combination of UCM and PBL schemes to examine its ability to replicate the diurnal cycle of T_{2m} in the Kansas City urban core. The YSU scheme was only paired with SLUCM since it is incompatible with BEP+BEM, resulting in a total of five runs. Simulations were initialized at 1200 UTC 19 July, 2012 and continued through 0000 UTC 24 July, which was during a period of elevated heat during which daytime highs averaged 37.9°C and nighttime lows averaged 25.0°C. The first 12 hours of model output was removed to avoid issues with model spin-up, yielding a total of 96 hours of data for analysis.

To assess each WRF configuration, model output T_{2m} was compared against hourly measured values obtained from National Weather Service Automated Surface Observing System (ASOS) stations at two locations: the Kansas City Downtown Airport (KMKC) station, which lies within the Kansas City urban core at 39.1208°N, 94.5902°W, and the Lee's Summit Municipal Airport (KLXT) station, situated approximately 25.8 km to its southeast at 38.9604°N, 94.3753°W. These locations represent urban and non-urban areas within the region of focus, allowing for the assessment of the paired urban and PBL schemes.

Comparisons between modeled and observed T_{2m} during the four-day analysis period for the five sensitivity runs are shown for KMKC in Figure 2.6 and KLXT in Figure 2.7. The performance of each UCM-PBL pairing was evaluated using three model validation metrics: the mean absolute error (MAE), the root mean squared error (RMSE), and the Pearson correlation coefficient (PCC).

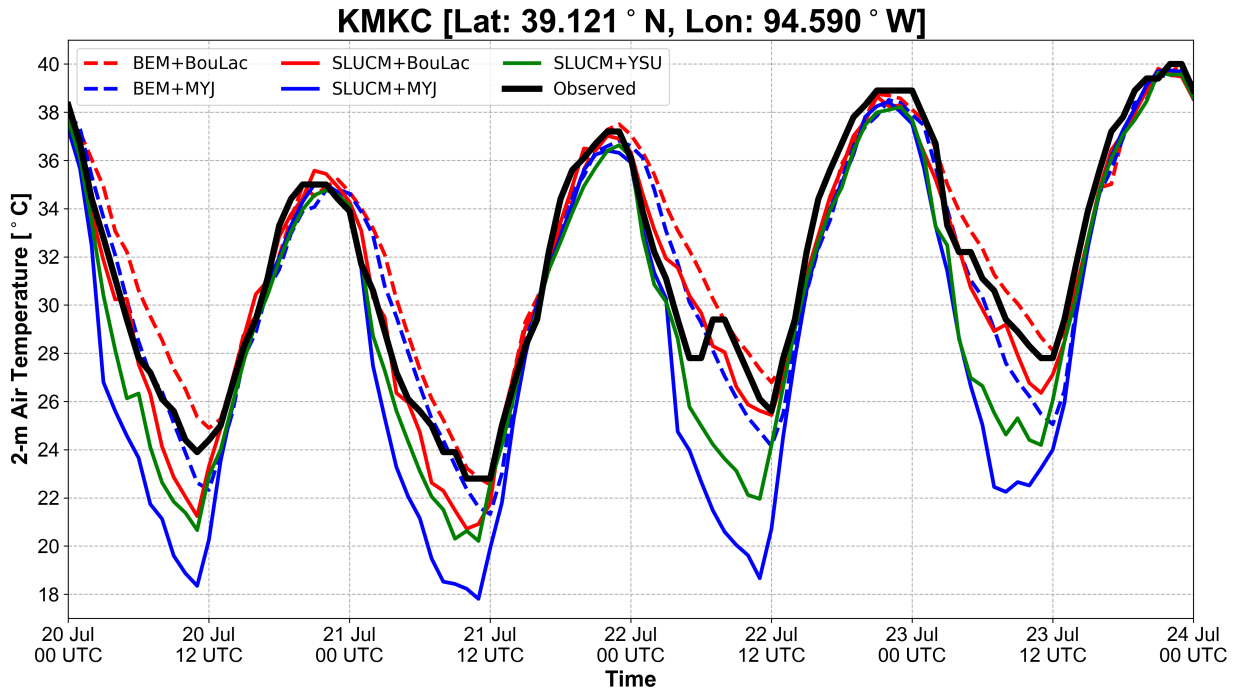

Figure 2.6: Hourly modeled 2-meter air temperature (T_{2m}) for each UCM+PBL configuration (colored) compared with observed values (black) for the period between 0000 UTC July 20 and 0000 UTC July 21, 2012 at the KMKC ASOS station.

Each of these parameters was calculated at both ASOS locations over all hours, and also for just daytime (13-01 UTC) and nighttime (02-12 UTC) periods. This allowed for the examination of WRF's ability to capture both the elevated high and low temperatures associated with UHIs, each which are critical individual factors contributing to heat-related illness and mortality in urban areas (Murage *et al.* 2017).

A summary of the validation statistics computed for both chosen locations and across the three time periods is presented in Table 2.2. The SLUCM+MYJ and SLUCM+YSU configurations both produced substantial nocturnal cold biases in the overnight hours, particularly in the urban setting of KMKC. While not the focus of this study, such an effect may have been caused by an inaccurate calculation of the surface energy balance or an under-representation of the turbulent mixing processes responsible for weaker surface inversions over urban areas. Regardless of source, the observed biases demonstrated that the aforementioned configurations were unable to sufficiently replicate the characteristically warm and well-mixed nocturnal urban boundary layer, thereby ren-

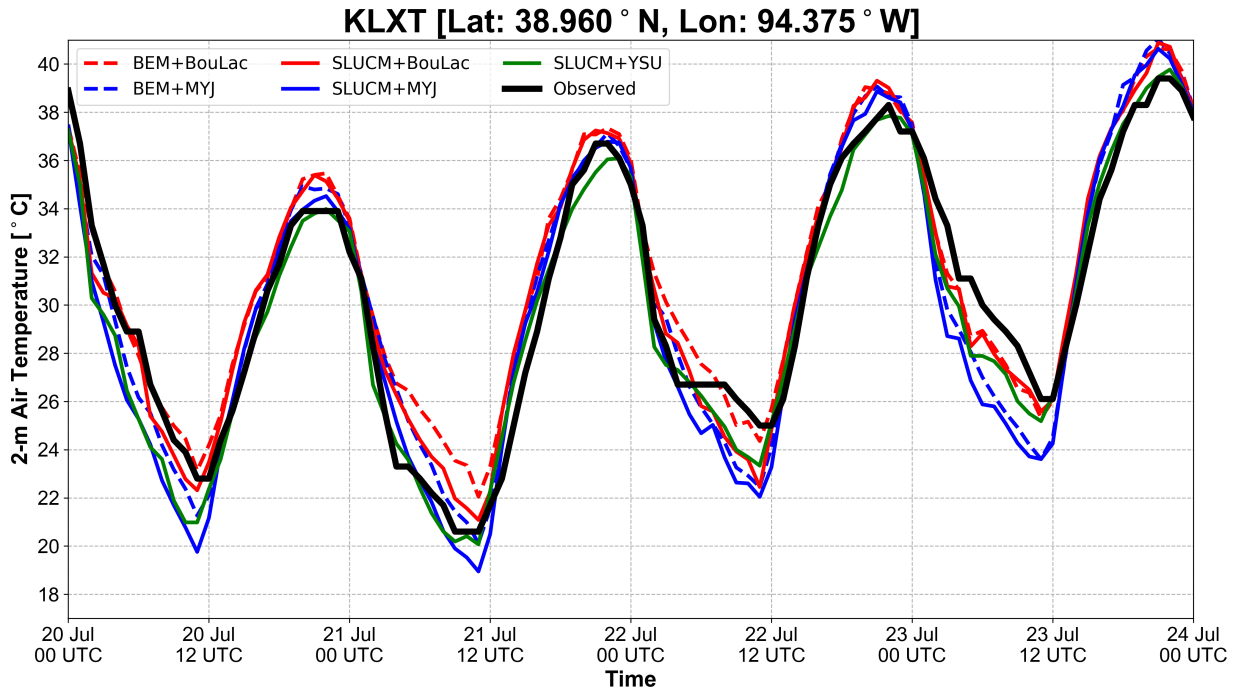

Figure 2.7: As in Figure 2.6, but for the KLXT ASOS location.

dering them inadequate for running simulations of the different greening scenarios. Conversely, the BEP+BouLac simulation produced a consistent warm bias during the nighttime period at KMKC. This indicated a tendency to overestimate UHII, which may again be associated with issues in the surface energy balance or turbulent mixing processes. Agreement between modeled and observed T_{2m} was better in the remaining two simulations, with RMSE values at both locations and all time periods falling within 2 °C. SLUCM+BouLac slightly outperformed BEP+MYJ by most metrics. Given the relatively strong performance of SLUCM+BouLac, the significantly less computational expense of SLUCM, and widespread use of SLUCM in current research, SLUCM+BouLac was selected to use in the experimental runs.

2.4 Overview of Experimental Simulations

To quantify the potential mitigation of Kansas City's UHI through urban greening, a series of experimental WRF simulations were performed. Three persistent periods of summertime heat

Table 2.2: Validation parameters computed using modeled and observed T_{2m} at the KMKC and KLXT ASOS stations for all WRF sensitivity runs. Parameters include: MAE (°C), RMSE (°C), and PCC (unitless). Calculations are performed over all times, daytime periods (13-01 UTC) and nighttime periods (02-12 UTC) to examine diurnal variation of model performance.

KMKC									
Configuration	**All**			**Day**			**Night**		
	RMSE	MAE	PCC	RMSE	MAE	PCC	RMSE	MAE	PCC
BEM+BouLac	1.48	0.61	0.96	0.89	-0.22	0.98	1.97	1.62	0.95
BEM+MYJ	1.37	-0.45	0.97	1.18	-0.68	0.98	1.56	-0.18	0.92
SLUCM+BouLac	1.12	-0.54	0.98	0.75	-0.33	0.99	1.45	-0.78	0.96
SLUCM+MYJ	3.68	-2.77	0.96	1.27	-0.94	0.98	5.28	-4.96	0.90
SLUCM+YSU	2.28	-1.75	0.97	0.98	-0.81	0.99	3.22	-2.89	0.91
KLXT									
Configuration	**All**			**Day**			**Night**		
	RMSE	MAE	PCC	RMSE	MAE	PCC	RMSE	MAE	PCC
BEM+BouLac	1.52	0.85	0.97	1.42	1.11	0.98	1.64	0.54	0.91
BEM+MYJ	1.59	-0.04	0.96	1.16	0.75	0.98	1.99	-1.00	0.87
SLUCM+BouLac	1.40	0.43	0.97	1.39	1.03	0.98	1.43	-0.29	0.92
SLUCM+MYJ	1.87	-0.64	0.96	1.04	0.53	0.98	2.54	-2.05	0.90
SLUCM+YSU	1.31	-0.64	0.98	0.82	-0.08	0.98	1.72	-1.32	0.95

with stagnant synoptic conditions were examined to avoid capturing the influence of convective and precipitation processes that introduce greater divergence of model solutions over time. Each case spanned a total of five days, beginning and ending at 0000 UTC: July 16-21, 2011, July 19-24, 2012, and August 24–30, 2013. While the region has been impacted by many other intense periods of heat in recent years, the selected cases were chosen due to their proximity to the publication of the geographic data used in the model system (2011) and the availability of NAM analysis data used to initialize WRF simulations.

WRF was run four times for the three examined cases. A summary of observed conditions during each case is presented in Table 2.3. The first simulation has no modifications to the input geographic datasets and provides a control simulation for each case. For the experimental

simulations, the previously calculated vacancy rate within the focus area of 28% was used to define three greening scenarios of varying intensity. These included a "conservative" strategy where half of available vacant space is converted to green space (14%), a "moderate" strategy where all available vacant space is converted (28%), and an "aggressive" strategy which accounts for the conversion of all available vacant land plus the greening of occupied spaces with features such as street trees, vegetation, and "green boulevards" (42%). Each model run spanned a total of 132 hours, with output saved hourly. The first 12 hours of output were again discarded from all analysis to avoid the model spin-up period, and all physics options were consistent with those utilized in the model sensitivity tests (Table 2.1).

Table 2.3: Overview of study periods for experimental WRF simulations, with simulation start and end dates (UTC) and mean observed T_{2m} (°C) at KMKC and KLXT for (13-01 UTC) and nighttime periods (02-12 UTC). Mean values for July-August are included for each site.

Case Study Periods

#	Period Start	Period End	KMKC		KLXT	
			$\overline{T}_{2m,\ day}$	$\overline{T}_{2m,\ night}$	$\overline{T}_{2m,\ day}$	$\overline{T}_{2m,\ night}$
1	2011-07-15, 12 UTC	2011-07-21, 00 UTC	33.7	29.5	33.3	28.2
2	2012-07-18, 12 UTC	2011-07-24, 00 UTC	34.8	28.7	33.8	27.3
3	2013-08-24, 12 UTC	2013-08-30, 00 UTC	32.2	26.8	30.3	24.9
July-August Mean, 2000-2018			**28.0**	**24.3**	**27.3**	**23.0**

A total of 251 model grid points within d03 were located within the focus area, encompassing a total area of 22.59 km^2. Input geographic datasets were modified to represent widespread greening within this area. Fractional LANDUSEF values for each of the three NLCD urban categories (24, 25, and 26) were reduced by 14%, 28%, and 42% for the conservative, moderate, and aggressive greening strategies respectively and were replaced by NLCD category 14 ("Cropland/Natural Vegetation Mosaic") to reflect the conversion of the abandoned area to diverse green spaces in the urban environment. Land use categories were subsequently re-calculated, and the value of LU_INDEX at each point was updated if necessary.

Values for FRC_URB2D and IMPERV within the area were proportionally reduced by the sum of all reduced urban fractional values to account for the loss of impervious surfaces due to greening, while CANFRA values were proportionally increased to represent the expansion of the tree canopy. A summary of mean values for relevant geographic input parameters within the focus area during the control run and each greening strategy is presented below in Table 2.4. All modifications made to input datasets were identical for each of the three test cases.

Table 2.4: Mean values for input WRF geographic parameters for control simulations (CTL) and simulations reflecting the conservative (CON), moderate (MOD) and aggressive (AGR) greening strategies.

Mean Geographic Input Parameters, Focus Area

Input Parameter	**CTL**	**CON**	**MOD**	**AGR**
LANDUSEF, Developed Low Intensity	0.42	0.36	0.30	0.24
LANDUSEF, Developed Medium Intensity	0.39	0.33	0.28	0.23
LANDUSEF, Developed High Intensity	0.10	0.08	0.07	0.06
LANDUSEF, Cropland/Natural Vegetation Mosaic	0.00	0.06	0.12	0.18
Total Urban Fraction (FRC_URB2D)	0.64	0.58	0.52	0.46
Impervious Surface Fraction (IMPERV)	0.47	0.33	0.19	0.09
Canopy Fraction (CANFRA)	0.12	0.19	0.26	0.33

Although the modifications made to the urban landscape in the three scenarios are not sweeping, they do represent levels of greening which could be realistically adopted in the focus area while also preserving the form and functionality of its neighborhoods. Furthermore, given the significant time and capital investments required to implement greening strategies on a large spatial scale, the strategies presented here offer a more practical outlook on potential UHI mitigation than other past studies of this manner (e.g. Zhou & Shepherd 2010; Morini *et al.* 2016; Fu & Weng 2017). While the social and political intricacies of urban greening are beyond the scope of this study, it is nonetheless hoped that the results of these simulations can be interpreted by decision makers as a baseline to establish future planning goals and strategies.

Chapter 3

Simulation Results

3.1 Overview

To assess the introduction of green spaces as a means of UHI mitigation within the focus area and thereby address the objectives of this project, three main aspects of the simulation results are presented here. To obtain an initial understanding of the WRF-resolved UHI at a higher resolution than previous numerical studies, the baseline characteristics of the simulated Kansas City UHI were examined. Following this, both the local the and non-local cooling impacts of urban greening within the model system were quantified. By doing so, it was possible to assess how urban greening policies could serve to reduce excessive urban heat within an economically and socially underserved region. Thus, we provide an initial justification for urban greening which ultimately may be utilized by planners and physical scientists alike to develop effective ways to develop ways to better predict and mitigate the impacts of the UHI.

As a baseline example of how the UHI is resolved by WRF for this study's simulations, mean T_{2m} values from the control simulation of Case 1 (July 16-21, 2012) are given for the daytime and nighttime periods in Figures 3.1A and 3.2A, respectively. An observable UHI is present over both periods over the Kansas City urban core, while mean T_{2m} values in the more forested suburban areas surrounding it are generally lower. Although urban greening in this study is not enacted where T_{2m} appears to be most enhanced by the UHI, the focus area lies within a region prone to its effects. We thus quantified the local impact of urban greening by comparing the distributions of T_{2m} values within the area and their variation based on strategy and the diurnal cycle. While local cooling is the most direct effect of land use conversion, Oliveira *et al.* 2011 and Declet-Barreto *et al.* 2013

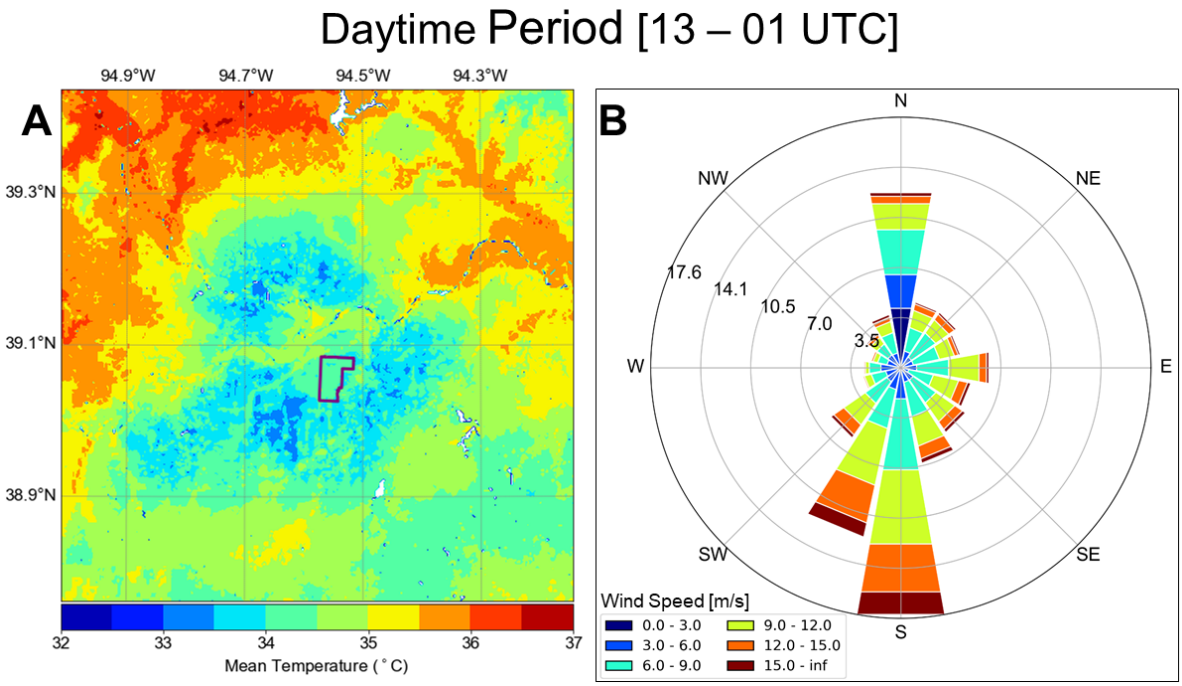

Figure 3.1: (A) Mean T_{2m} values (°C, shaded contours) for d03 over the daytime period (13-01 UTC) between 16 July - 21 July, 2012 (Case Study 1), with focus area highlighted (purple). (B) Daytime wind climatology (m/s) for July and August at KMCI, derived from hourly surface observations between 2000-2018.

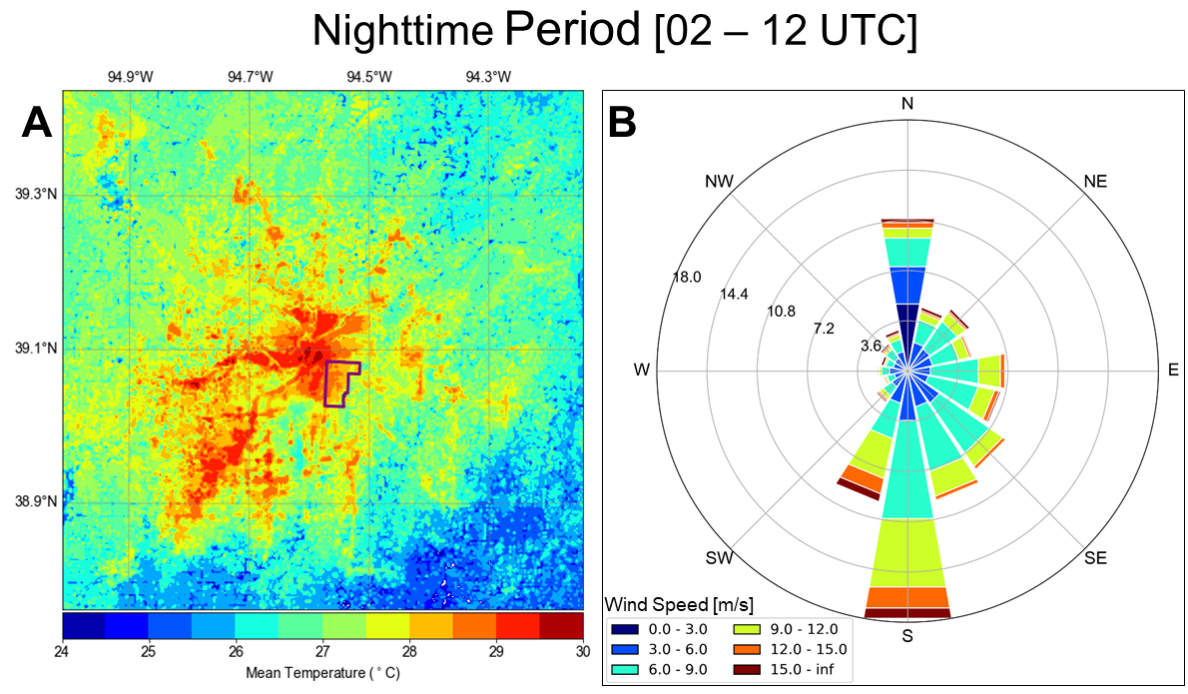

Figure 3.2: (A) As in Figure 3.1A, but for the nighttime period (02-12 UTC). (B) As in Figure 3.1B, but for the nighttime period (02-12 UTC).

have also demonstrated the benefits of downwind advective cooling in areas surrounding of urban green spaces. Kansas City's summertime wind climatology (Figures 3.1B and 3.2B) suggests that cooler air associated with implemented green spaces is likely to be transported towards the residential area north of the focus region, which exhibits a similar pattern of high vacancy rates (Figure 2.2). Given the additional health benefits that this process may provide, downwind cooling was also analyzed to further highlight the strengths of urban greening in reducing UHI impacts.

3.2 Characteristics of the Simulated Kansas City UHI

For each of the three control WRF simulations, the composition of the resolved Kansas City UHI was assessed for the daytime (13-01 UTC, 8 AM – 9 PM local time) and nighttime (02-12 UTC, 9 PM – 8 AM local time) periods by quantifying the relationship between mean model derived T_{2m} and the total urban fraction dataset generated by WPS (FRC_URB2D). The linearity of this relationship was examined by creating density plots for all cases, binned at 0.1 °C increments for temperature and 1% increments for urban fraction (Figure 3.3). Because non-urban grid cells represent a majority of the overall land area within the innermost model domain (65.9%), all points with an urban fraction below 10% were removed from this analysis to reduce the potentially large influence of rural temperature variability. In addition, to provide a metric for comparison between simulations and time periods, the Pearson Correlation Coefficient (r) was derived between mean air temperature and urban fraction for each plot.

A weak to moderate positive relationship between T_{2m} and urban fraction indicative of the UHI was observable across all cases. However, PCC values were noticeably greater and trend line slopes sharper in each case over the nighttime period. This was particularly evident across Case 1, during which a relatively strong positive correlation was present during the night ($r = 0.75$) while no relation between the two variables was observed during the day ($r = 0.02$). A similar pattern was visible across the remaining control runs, although the daytime T_{2m} – urban fraction relationship was more positively correlated for Case 2 ($r = 0.53$) and Case 3 ($r = 0.32$).

The Kansas City UHI resolved by the control simulations was consistent in structure and diur-

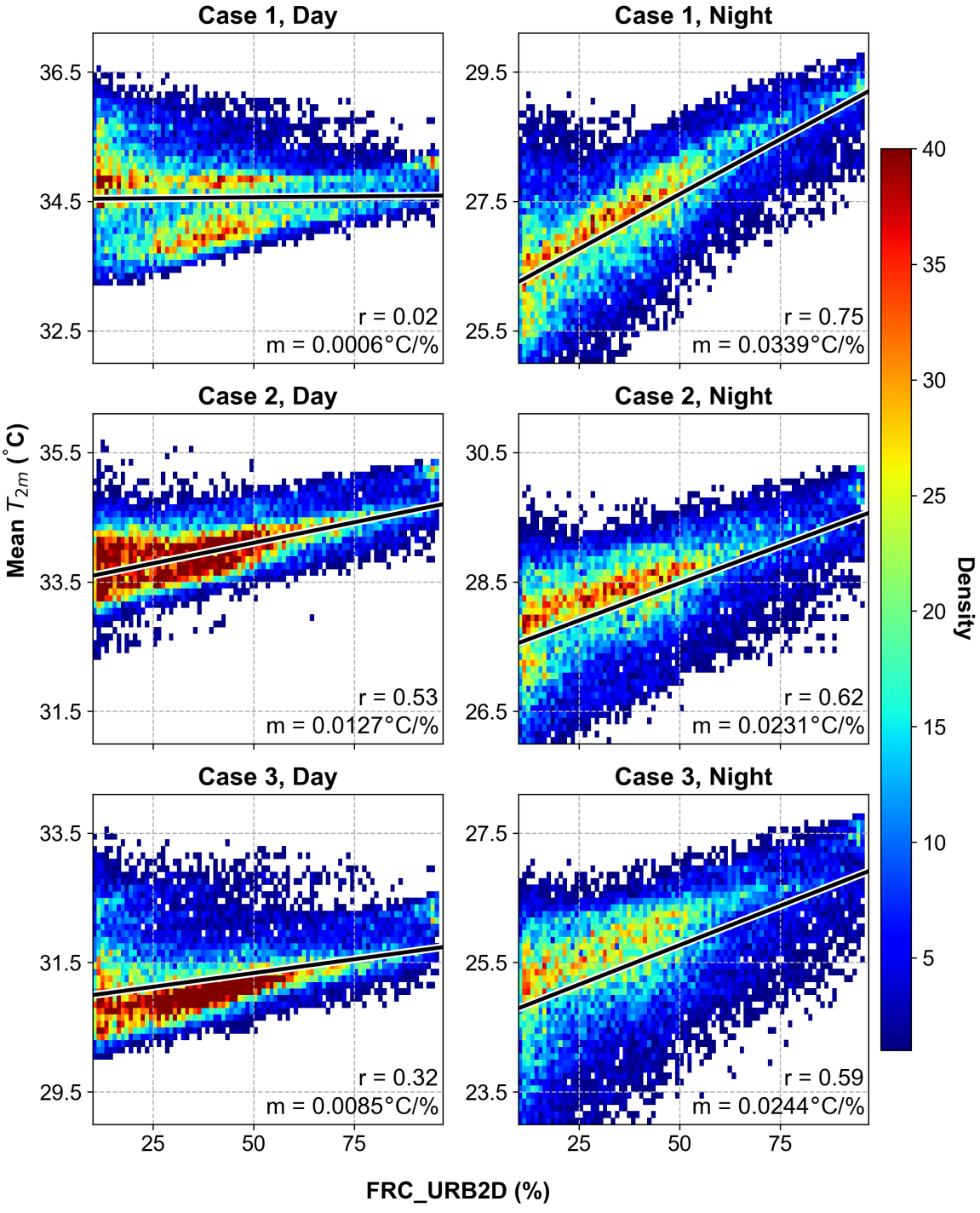

Figure 3.3: Density plots relating mean T_{2m} values (°C) and FRC_URB2D (%) across the daytime (13-01 UTC) and nighttime (12-02 UTC) periods for the control simulations. Values are binned by 0.1°C increments for air temperature and 1% increments for urban fraction. The PCC (r) and slope for the temperature-urban fraction relationship are included for each plot.

nal variation with numerous previous observational studies at other locations, such as Tran *et al.* 2006, Azevedo *et al.* 2016, and Tan *et al.* 2010. By utilizing an inner model domain with roughly block-level resolution and detailed LULC data, WRF was able to replicate the inhibited radiative cooling rates overnight commonly seen in heterogeneous urban landscapes and thus produce the stronger and more distinct UHI associated with synoptically stagnant summer evenings. Given the dependency of the urban nocturnal boundary layer on local heat fluxes identified in Halios & Barlow 2018, this assertion could further be supported by analyzing the surface energy budget within the study area produced by WRF. However, this prospect is limited by a lack of observational data available over the study area at sufficient spatial and temporal frequency to directly validate model representation of the surface energy budget.

To further investigate the diurnal evolution of the UHI in the control simulations, hourly modeled UHII was analyzed for each of the case studies and is presented in Figure 3.4. In a similar manner to the model validation process, UHII was calculated as the difference in T_{2m} between the KMKC (urban) and KLXT (non-urban) ASOS locations. In accordance with the previous analyses, the simulated UHI exhibits a clear periodicity across all three cases, peaking in intensity at approximately 03 UTC (10 PM local time) and reaching a minimum at approximately 14 UTC (9 AM local time). Mean UHII for all simulations was 1.44 °C during the daytime hours and 0.61 °C overnight, although maximum nighttime values at times reached upwards of 4 °C. The UHII was occasionally negative, most notably during the daytime periods of Case 1. This so-called "urban cool island" has been observed to occur during the day in other locations, is usually fairly weak, and is attributed to factors such as higher thermal inertia in urban areas as compared to rural areas (Bohnenstengel *et al.* 2011).

Next, to assess air temperature variability across the diverse LULC settings of the model grid, daytime and nighttime mean temperature distributions were visualized across the control simulations for each grid point's dominant NLCD land use classification (Figure 3.5). An exception was grid points where NLCD category 21 (Open Water) was dominant, which was removed from analysis due to its comparatively low number within the innermost domain. Across both time periods

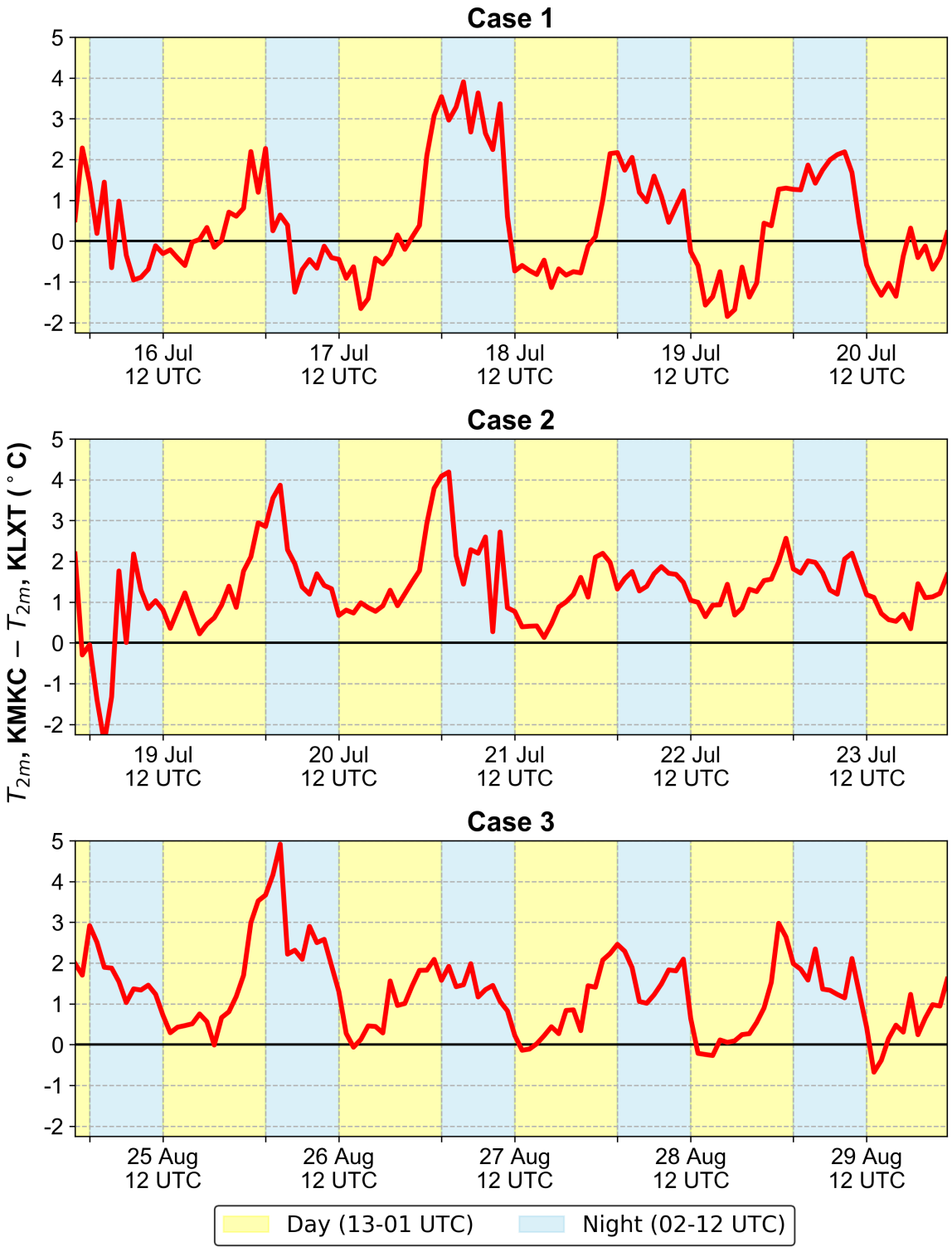

Figure 3.4: Hourly modeled UHII (°C) for each case study, calculated as the difference in simulated T_{2m} at the KMKC and KLXT locations. Daytime and nighttime periods are highlighted in yellow and blue, respectively.

and all cases, the distributions of T_{2m} in grid cells where urban land use was dominant (NLCD categories 23 – 26) expectedly and consistently showed an increase in both mean and median T_{2m} with increased urban density. Urban-classified cells showed little to no UHI signal during the daytime period when compared with forested, agricultural, and wetland areas, likely due to the aforementioned "cool island". Wetland areas (NLCD categories 39 and 40) were shown to be particularly warmer during the daytime period, although the spatial distribution of points with these classification was limited to only a few locations within the inner domain (2.1). This is likely attributable to the higher emissivity and thermal inertia of these areas compared to other natural land cover categories (Appendix A).

Over the nighttime periods, greater mean, median, and quartile T_{2m} values were observed for urban-dominant cells when compared to other categories. The range of values in these locations, however, was much wider than those during the day periods. Given that the model system uses fractional land use values to calculate T_{2m} instead of the simpler categorical LU_INDEX array, some of this variability may be in part due to the scattered presence of less-dominant LULC types in grid cells with dominant urban cover. Another potential key factor in nighttime temperature variability is the formation of the stable nocturnal boundary layer, which coincides with a reduction in turbulent mixing and vertical heat and momentum transport, which can feed back into surface cooling rates and thus result in a greater sensitivity of local air temperatures to surrounding land cover characteristics. Considering these factors, it is likely from these simulations and past observations that implemented green spaces would have a greater impact on reducing overnight lows than daytime highs. Although this may not serve as a significant means of mitigating the extreme *daytime* high temperatures associated with an array of public health concerns, a cooler temperature *overnight* has been identified as a critical factor in reducing heat-related illnesses and morbidity in urban areas (e.g. Murage *et al.* 2017; Frumkin 2002).

Overall, the control simulations demonstrate WRF's ability to reproduce the thermal structure of the UHI, consistent with observed trends in its diurnal evolution and sensitivity to varying LULC qualities (e.g., Estoque 2017). The control runs additionally show the value of increasing the inner

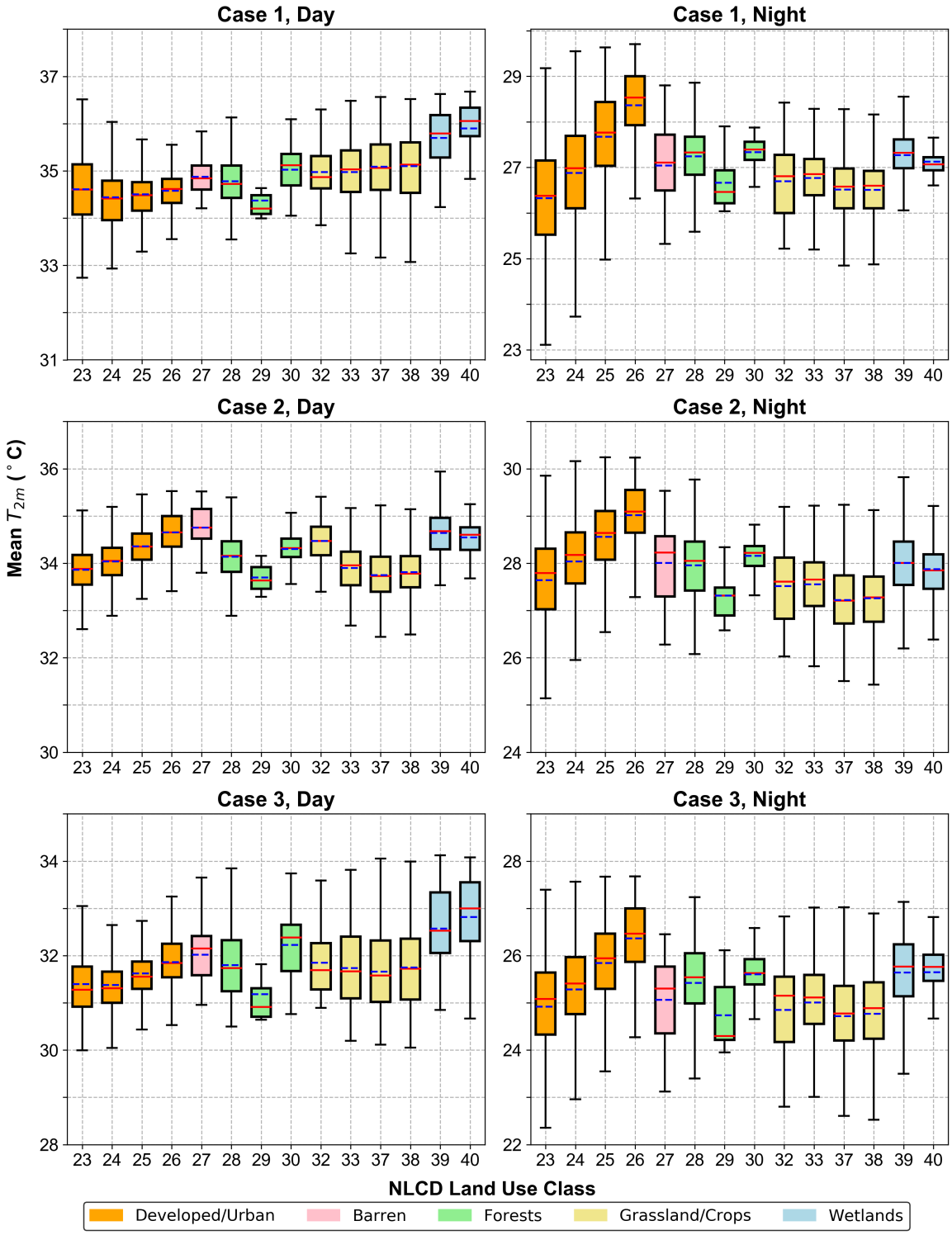

Figure 3.5: Distribution of mean daytime (left) and nighttime (right) T_{2m}, delineated by NLCD Land Use classification, for all three control simulations. Mean (red, solid) and median (blue, solid) values are highlighted for each distribution. Land use category information and properties can be found in Appendix A.

domain resolution beyond levels typically found in other UHI simulations using WRF, which will allow the experimental greening simulations to be performed and analyzed with greater confidence.

3.3 Local Impacts of Urban Greening

Values for ΔT_{2m} were obtained for all cases and greening strategies by calculating the difference in 2-meter air temperature between each case's control simulation and the three experimental runs (i.e., Experimental ΔT_{2m} − Control ΔT_{2m})). In doing so, it was possible to quantify the potential mitigation of the UHI from the prescribed conversion of current vacant lots to green spaces during both the daytime and nighttime by examining the distribution of ΔT_{2m} within the focus area. The analyses in this section offer a simple and relatively direct assessment of the potential utility of greening as an avenue to potential UHI mitigation. Figure 3.6 depicts ΔT_{2m} after sunset (03 UTC) for Case 1. Small scale differences between the experimental and control runs are prevalent throughout the domain and are associated with the turbulent nature of the lower atmosphere. Despite the noisy background at this single time, there is a clear cooling signal within the focus area. This depiction exemplifies the cooling effect which was observable to varying degrees across all cases and greening magnitudes. To provide an assessment of the projected impacts of urban greening within the focus area itself, the temporal evolution of ΔT_{2m} for each strategy and case was assessed by examining its distribution across the diurnal cycle. A visualization of this analysis for the three simulation cases and greening strategies is depicted in Figure 3.7.

While the impacts of simulated urban greening exhibited substantial variation across greening strategies and over the diurnal cycle, the modifications made to land cover within the focus area in the model system nonetheless resulted in a general reduction of local 2-meter air temperature as expected. The cooling associated with these modifications was most apparent from approximately 04-15 UTC (11 PM – 10 AM local time) across the three cases, encompassing the majority of the overnight and early morning period where atmospheric UHII has previously been observed to be greatest (e.g. Voogt 2007, Azevedo *et al.* 2016). For Case 1, cooler ΔT_{2m} values extended further into the daytime period, with median cooling values greater than 0.70°C through 22 UTC in the

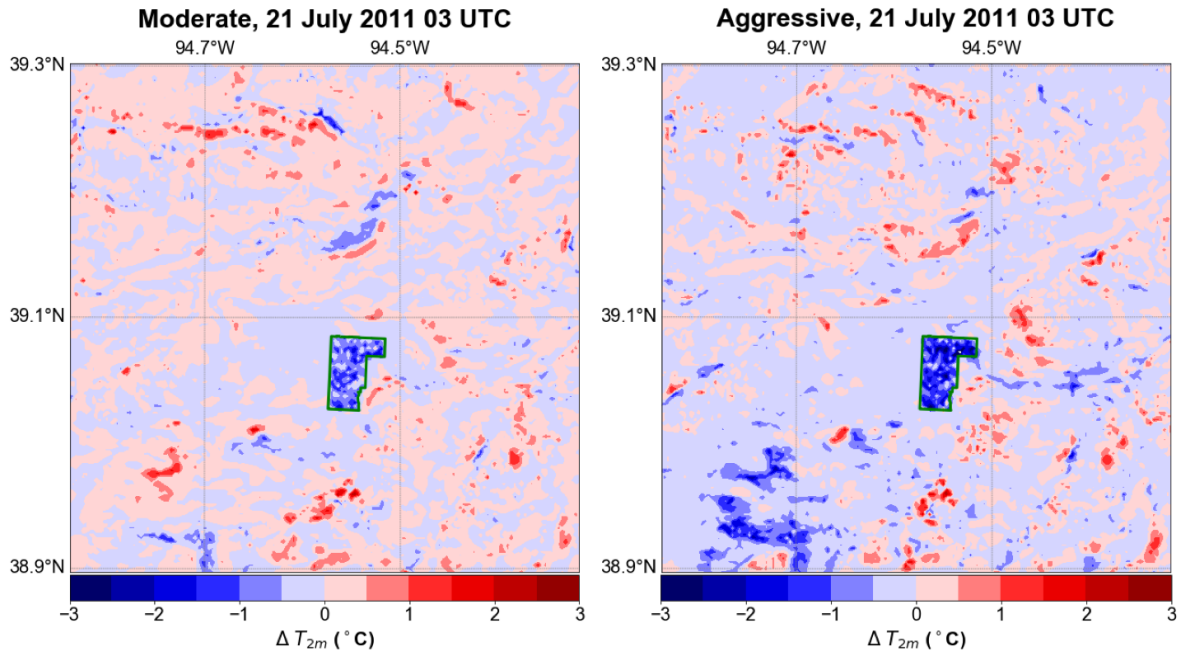

Figure 3.6: ΔT_{2m} values (shaded contours, °C) at 03 UTC 21 July 2011 for the moderate (left) and aggressive (right) greening strategies. The focus area is denoted with a green outline.

aggressive greening scenario. The effects of land use conversion were generally smaller during the daytime period. This was likely attributable to increased thermal mixing driven by turbulent motion within the boundary layer.

The diurnal cycle of surface sensible and latent heat fluxes within the focus area for each level of greening (Figure 3.8) aligns well with the the anticipated impacts of new green spaces on both the surface energy balance and the resultant 2-meter air temperature. Within the previously established daytime period (12-02 UTC), the introduction of additional vegetation into the focus area results in an increase in upward latent heat flux which appears to scale linearly based on the extent of the introduced green spaces. This variation reached upwards of 100 Wm^{-2} between the control and aggressive greening simulations for each case. Concurrently, the increase of daytime latent heating proportionally reduced upward sensible heat flux over the same time period, ultimately resulting in a more rapid and stronger cooling of 2-meter temperatures after sunset (02-12 UTC). Within the daytime boundary layer, on the other hand, the effect of this shift on T_{2m} is ultimately negligible due to the dominance of deep and thorough turbulent mixing processes. This

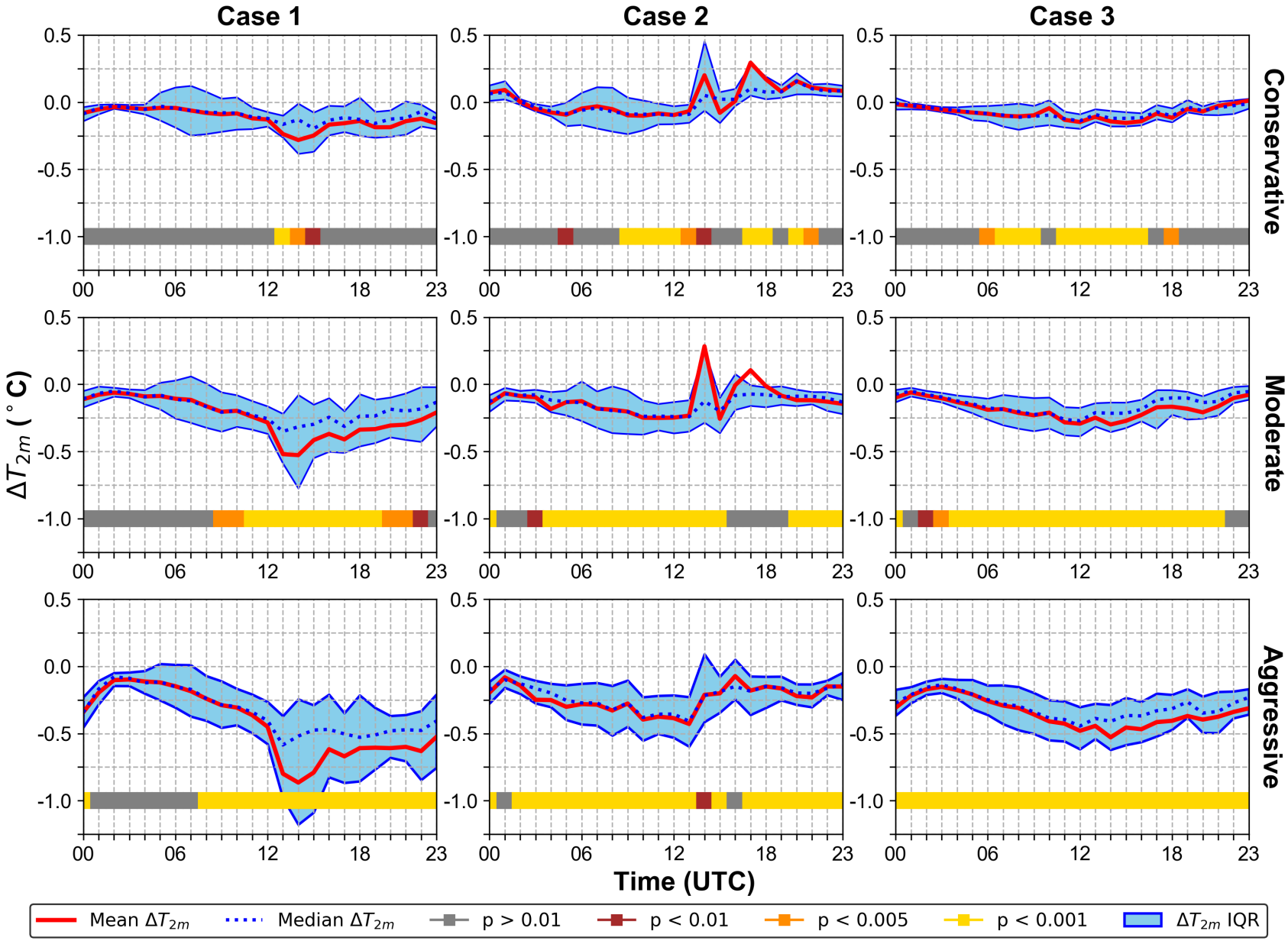

Figure 3.7: Analysis of the ΔT_{2m} distribution within the focus area for the each cases and strategy, consisting of ΔT_{2m} values at all grid points inside of the area binned by hour (UTC). Shown for each simulation are the mean (red), median (blue) and interquartile range (blue shaded) of the ΔT_{2m} distribution at each hour. Statistical significance of the simulated cooling is denoted at the the $p < 0.01$ (brown), $p < 0.005$ (orange), and $p < 0.001$ (yellow) levels.

is in agreement with the conceptual urban energy balance presented in Oke 1988, which can be confirmed with ground truth by the reductions in nighttime temperatures surrounding urban green spaces previously observed in studies such as Oliveira *et al.* 2011 and Feyisa *et al.* 2014.

The magnitude of local nocturnal cooling in the conservative greening simulations was minimal, as mean and median ΔT_{2m} values rarely exceeded -0.25 °C and positive ΔT_{2m} values were often captured within the interquartile range of the distribution. While expected given the impacts of land use conversion on the modeled surface energy balance, simulations carried out using moderate and aggressive greening strategies produced a more noticeable nocturnal cooling signal. Mean and median hourly ΔT_{2m} values during the overnight period generally surpassed -0.25 °C for moderate greening simulations and -0.50 °C for aggressive greening simulations. Furthermore, the interquartile range of the moderate and aggressive ΔT_{2m} distributions rarely captured any positive values during the overnight hours. As a whole these results suggest that at least the moderate scenario must be implemented to have any impact at all and the extent of land use conversion in an urban greening strategy must be relatively significant to produce meaningful heat mitigation impacts. This study was constrained by limiting the changes to *existing* abandoned lots, but still found that there is an impact for converting these abandoned properties to green spaces. So this is a viable method of reducing elevated atmospheric temperatures attributed to the UHI by a significant, albeit not large, amount.

Hourly median and 75th percentile ΔT_{2m} values for cases 1, 2, and 3 are presented in Tables 3.1, 3.2, and 3.3, respectively. To further quantify whether the potential cooling effects of urban greening within the model system were in fact meaningful, it was also necessary to perform statistical significance tests on the obtained ΔT_{2m} datasets for each case. To do so, a two-sample Student's t-test was performed between the control and experimental simulations at each hour and for each case and greening strategy. In obtaining the resultant p-values from these tests, it was possible to determine when and under what extent of greening the land use conversion produced a statistically significant cooling signal. In addition to being listed in the tables 3.1, 3.2, and 3.3, the results of the t-tests are also denoted in Figure 3.7.

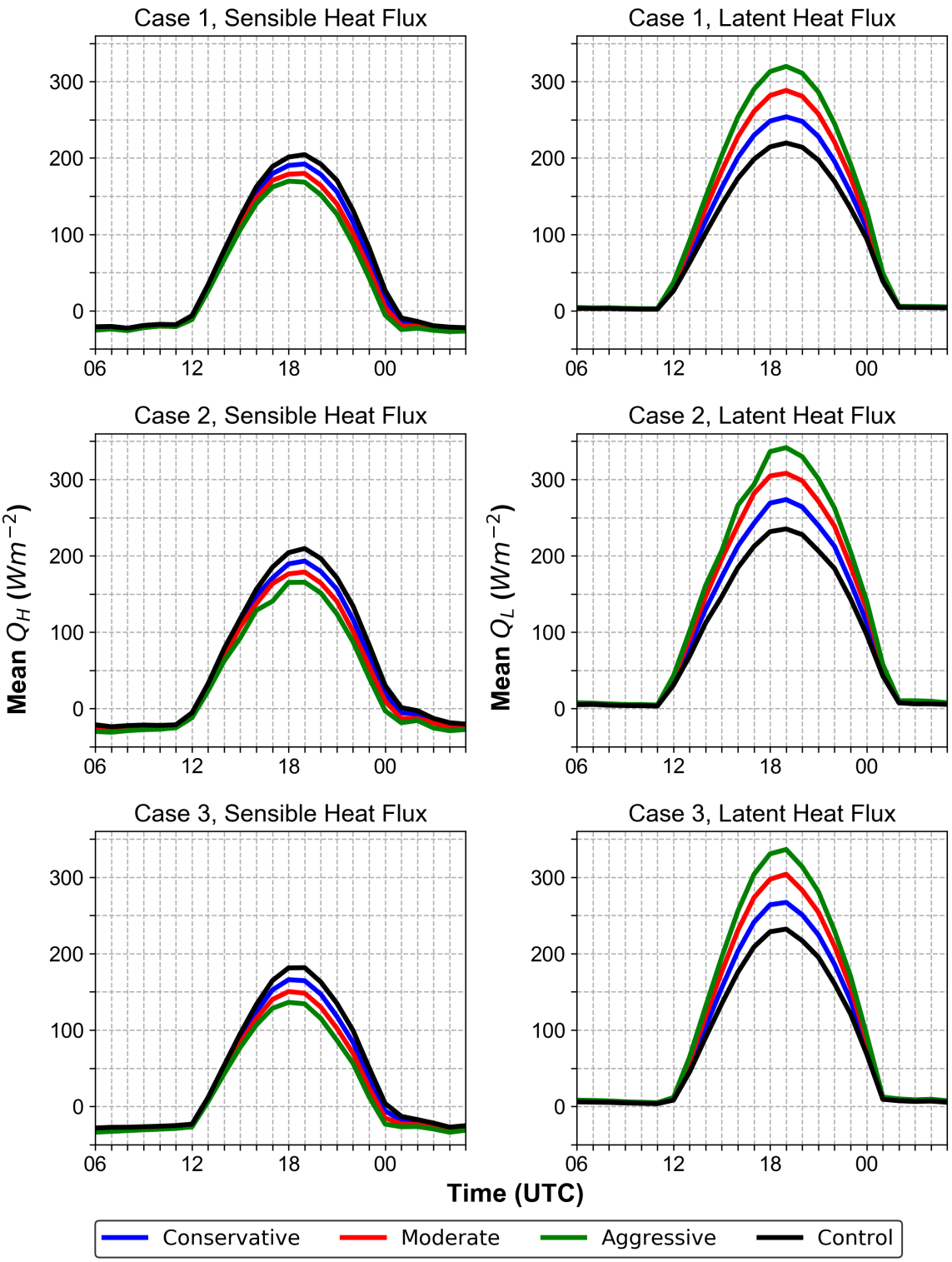

Figure 3.8: Mean surface sensible (left) and latent (right) heat fluxes (Wm^{-2}) within the focus area for the control (black, solid), conservative (blue, solid), moderate (red, solid), and aggressive (green, solid) simulations for each of the three cases.

Table 3.1: Median (Q50) and 75th percentile (Q75) ΔT_{2m} values (°C) for the three Case 1 simulations, binned by hour (UTC). The statistical significance of each hourly distribution is given via the p-value obtained from performing a Student's t-test between the control and experimental data. Results significant at the 0.01 (*), 0.005 (**), and <0.001 (***) levels are denoted with asterisks.

ΔT_{2m}: Case 1 (July 16-21, 2011)

	Conservative			**Moderate**			**Aggressive**		
T	**Q50**	**Q75**	***p*-value**	**Q50**	**Q75**	***p*-value**	**Q50**	**Q75**	***p*-value**
00	-0.09	-0.14	0.332	-0.11	-0.17	0.180	-0.34	-0.45	<0.001***
01	-0.04	-0.09	0.490	-0.07	-0.13	0.312	-0.17	-0.28	0.011
02	-0.03	-0.05	0.638	-0.05	-0.09	0.399	-0.07	-0.14	0.165
03	-0.04	-0.07	0.568	-0.07	-0.10	0.346	-0.09	-0.14	0.200
04	-0.05	-0.09	0.552	-0.09	-0.15	0.282	-0.12	-0.20	0.179
05	-0.03	-0.13	0.616	-0.08	-0.18	0.299	-0.11	-0.25	0.156
06	-0.05	-0.19	0.589	-0.11	-0.25	0.172	-0.15	-0.31	0.060
07	-0.06	-0.25	0.400	-0.12	-0.29	0.114	-0.17	-0.37	0.012
08	-0.07	-0.24	0.267	-0.16	-0.32	0.023	-0.24	-0.40	<0.001***
09	-0.08	-0.22	0.179	-0.21	-0.35	0.002**	-0.28	-0.45	<0.001***
10	-0.08	-0.20	0.213	-0.19	-0.31	0.003**	-0.30	-0.44	<0.001***
11	-0.11	-0.20	0.071	-0.23	-0.34	<0.001***	-0.34	-0.50	<0.001***
12	-0.12	-0.18	0.010*	-0.26	-0.37	<0.001***	-0.40	-0.58	<0.001***
13	-0.16	-0.26	<0.001***	-0.35	-0.59	<0.001***	-0.58	-0.98	<0.001***
14	-0.13	-0.38	0.003**	-0.32	-0.77	<0.001***	-0.52	-1.18	<0.001***
15	-0.20	-0.37	0.009*	-0.30	-0.55	<0.001***	-0.47	-1.09	<0.001***
16	-0.13	-0.24	0.068	-0.24	-0.50	<0.001***	-0.47	-0.82	<0.001***
17	-0.11	-0.22	0.067	-0.31	-0.51	<0.001***	-0.50	-0.87	<0.001***
18	-0.13	-0.25	0.109	-0.24	-0.46	<0.001***	-0.53	-0.85	<0.001***
19	-0.16	-0.26	0.041	-0.24	-0.44	<0.001***	-0.51	-0.77	<0.001***
20	-0.13	-0.25	0.042	-0.18	-0.39	0.001**	-0.48	-0.68	<0.001***
21	-0.12	-0.24	0.155	-0.20	-0.41	0.003**	-0.47	-0.71	<0.001***
22	-0.06	-0.18	0.188	-0.18	-0.43	0.005*	-0.48	-0.84	<0.001***
23	-0.13	-0.20	0.098	-0.13	-0.31	0.032	-0.41	-0.75	<0.001***

Table 3.2: As in Table 3.1, but for ΔT_{2m} distributions for Case 2.

ΔT_{2m}: Case 2 (July 19-24, 2012)

	Conservative			**Moderate**			**Aggressive**		
T	**Q50**	**Q75**	***p*-value**	**Q50**	**Q75**	***p*-value**	**Q50**	**Q75**	***p*-value**
00	0.06	0.01	0.060	-0.12	-0.20	<0.001***	-0.17	-0.28	<0.001***
01	0.07	0.02	0.019	-0.07	-0.12	0.091	-0.10	-0.16	0.035
02	0.00	-0.01	0.937	-0.08	-0.12	0.018	-0.13	-0.20	<0.001***
03	-0.03	-0.07	0.145	-0.08	-0.14	0.005*	-0.16	-0.27	<0.001***
04	-0.06	-0.10	0.024	-0.12	-0.21	<0.001***	-0.20	-0.30	<0.001***
05	-0.08	-0.18	0.007*	-0.13	-0.23	<0.001***	-0.25	-0.40	<0.001***
06	-0.06	-0.17	0.110	-0.14	-0.27	<0.001***	-0.27	-0.43	<0.001***
07	-0.04	-0.19	0.248	-0.18	-0.32	<0.001***	-0.27	-0.44	<0.001***
08	-0.07	-0.22	0.015	-0.19	-0.36	<0.001***	-0.32	-0.51	<0.001***
09	-0.09	-0.24	<0.001***	-0.20	-0.37	<0.001***	-0.27	-0.45	<0.001***
10	-0.09	-0.21	<0.001***	-0.24	-0.37	<0.001***	-0.38	-0.55	<0.001***
11	-0.09	-0.16	<0.001***	-0.24	-0.34	<0.001***	-0.36	-0.50	<0.001***
12	-0.10	-0.16	<0.001***	-0.13	-0.36	<0.001***	-0.36	-0.53	<0.001***
13	-0.09	-0.15	0.001**	-0.20	-0.35	<0.001***	-0.41	-0.60	<0.001***
14	0.05	-0.06	0.007*	-0.08	-0.28	<0.001***	-0.22	-0.41	0.006*
15	0.02	-0.15	0.124	-0.07	-0.36	<0.001***	-0.19	-0.34	<0.001***
16	0.02	-0.03	0.824	-0.08	-0.19	0.841	-0.15	-0.24	0.052
17	0.10	0.05	<0.001***	-0.07	-0.16	0.012	-0.19	-0.36	<0.001***
18	0.07	0.02	<0.001***	-0.08	-0.17	0.700	-0.15	-0.31	<0.001***
19	0.08	0.03	0.014	-0.09	-0.15	0.010*	-0.16	-0.25	<0.001***
20	0.15	0.06	<0.001***	-0.09	-0.16	<0.001***	-0.20	-0.28	<0.001***
21	0.10	0.06	0.001**	-0.09	-0.15	<0.001***	-0.20	-0.30	<0.001***
22	0.08	0.05	0.001**	-0.10	-0.20	<0.001***	-0.16	-0.21	<0.001***
23	0.08	0.04	0.012	-0.13	-0.22	<0.001***	-0.13	-0.25	<0.001***

Table 3.3: As in Table 3.1, but for ΔT_{2m} distributions for Case 3.

ΔT_{2m}: Case 3 (August 25-30, 2013)

	Conservative			Moderate			Aggressive		
T	**Q50**	**Q75**	***p*-value**	**Q50**	**Q75**	***p*-value**	**Q50**	**Q75**	***p*-value**
00	-0.01	-0.05	0.603	-0.07	-0.13	0.001**	-0.27	-0.37	<0.001***
01	-0.03	-0.05	0.297	-0.05	-0.09	0.021	-0.21	-0.27	<0.001***
02	-0.04	-0.05	0.200	-0.07	-0.11	0.006*	-0.15	-0.21	<0.001***
03	-0.05	-0.07	0.107	-0.09	-0.13	0.003**	-0.14	-0.20	<0.001***
04	-0.06	-0.09	0.067	-0.12	-0.17	<0.001***	-0.17	-0.24	<0.001***
05	-0.07	-0.13	0.022	-0.14	-0.21	<0.001***	-0.21	-0.32	<0.001***
06	-0.08	-0.14	0.004**	-0.18	-0.26	<0.001***	-0.25	-0.36	<0.001***
07	-0.10	-0.18	<0.001***	-0.19	-0.30	<0.001***	-0.28	-0.43	<0.001***
08	-0.11	-0.20	<0.001***	-0.20	-0.33	<0.001***	-0.29	-0.47	<0.001***
09	-0.11	-0.18	0.002**	-0.23	-0.35	<0.001***	-0.34	-0.50	<0.001***
10	-0.10	-0.17	<0.001***	-0.21	-0.33	<0.001***	-0.38	-0.55	<0.001***
11	-0.12	-0.19	<0.001***	-0.26	-0.38	<0.001***	-0.40	-0.56	<0.001***
12	-0.14	-0.20	<0.001***	-0.27	-0.39	<0.001***	-0.44	-0.62	<0.001***
13	-0.09	-0.14	0.001**	-0.21	-0.31	<0.001***	-0.39	-0.54	<0.001***
14	-0.12	-0.18	<0.001***	-0.21	-0.35	<0.001***	-0.41	-0.62	<0.001***
15	-0.12	-0.18	<0.001***	-0.21	-0.32	<0.001***	-0.36	-0.59	<0.001***
16	-0.11	-0.17	<0.001***	-0.18	-0.27	<0.001***	-0.37	-0.56	<0.001***
17	-0.07	-0.12	0.010	-0.11	-0.33	<0.001***	-0.33	-0.52	<0.001***
18	-0.10	-0.15	0.002**	-0.10	-0.22	<0.001***	-0.31	-0.47	<0.001***
19	-0.04	-0.07	0.251	-0.10	-0.26	<0.001***	-0.26	-0.38	<0.001***
20	-0.06	-0.09	0.204	-0.13	-0.25	<0.001***	-0.35	-0.49	<0.001***
21	-0.04	-0.09	0.542	-0.13	-0.23	<0.001***	-0.34	-0.50	<0.001***
22	-0.02	-0.09	0.803	-0.06	-0.14	0.011	-0.27	-0.39	<0.001***
23	-0.01	-0.05	0.700	-0.05	-0.11	0.016	-0.23	-0.36	<0.001***

The cooling signals produced by the conservative simulations displayed few instances of statistical significance compared to the more aggressive scenarios. The moderate and aggressive greening scenarios tended to produce a widespread cooling signal which was significant at or below the $p = 0.001$ level. Within the moderate simulations, this level of significance was confined mostly to the overnight through early afternoon period, ranging from approximately 04-20 UTC across each of the three cases. Conversely, for the aggressive greening simulations, this period extended throughout the majority of the diurnal cycle. The results obtained from the significance tests here are by no means unexpected. They do however further reiterate that countering the negative ramifications of the UHI via land use conversion appears to only be effective in more extensive greening scenarios, which may require a more substantial investment that requires the use of significant social, financial, and political capital.

3.4 Downwind Impacts of Urban Greening

While the primary concern of this study was to examine the utility of land use conversion to provide local cooling effects as a means of UHI mitigation, observational studies such as Oliveira *et al.* 2011 and Chow *et al.* 2011 have demonstrated that reductions in near-surface air temperature associated with urban green spaces are not necessarily confined to just the converted spaces. As discussed in Doick *et al.* 2014, advective processes often result in an expansion of the "park cool island" in urban areas to surrounding non-vegetated areas. Like the observed diurnal cycle of cooling intensity within green spaces, the non-local effects of greening are also strongest during the nighttime. Given that these additional benefits of green space implementation may further justify the pursuit UHI abatement through land use conversion, it was important to examine the strength and extent of simulated downwind cooling surrounding the focus area for this study.

As shown in Figures 3.1 and 3.2, the synoptic flow over Kansas City is generally from the south in the summer months, so the north side is typically the downwind side. Furthermore, the block-level census data visualized in Figure 2.2 show additional locations to the north of the focus area with similarly high residential vacancy rates. Given that these areas exhibit similar characteristics

to the focus area and are located where cold air advection from the "park cool island" would be climatologically most frequent, the overarching UHI mitigation goals sought in this project could possibly extend beyond just the local areas with implemented green spaces. As a result, ΔT_{2m} was assessed across each case and greening scenario for model grid locations downwind from the boundaries of the focus area at each time step.

To determine the maximum advective cooling (an upper bound) in grid cells surrounding the focus area, it was necessary to determine which cells would be considered downwind from its boundaries at each time step. To do so, a unit vector oriented along the prevailing wind direction ($\hat{v}$) was obtained at the center of the focus area (39.059°N, 94.551°W or (113, 136) on the model grid) using the simulated u and v-components of the 10-meter wind speed as follows:

$$\hat{v} = \left(\frac{u}{\sqrt{u^2+v^2}}\right)\hat{i} + \left(\frac{v}{\sqrt{u^2+v^2}}\right)\hat{j} \tag{3.1}$$

Here, u and v are the components of the 10-meter wind vector and $\sqrt{u^2+v^2}$ is the magnitude of the 10-meter wind. Using this unit vector, model grid locations along a line parallel to the wind direction were found until a point at the edge of the focus area was reached. Points falling within a 45°arc extending 2 km from this boundary point and a 20°arc extending a further 8 km were considered "downwind" for the purpose of determining maximum advective cooling. This process is visualized in Figures 3.9 and 3.10. Once the downwind grid points were determined, the euclidean distance between each point and the edge of the focus area was calculated. The points were then binned at 0.2 km increments based on this distance. Finally, to quantify the degree of downwind cooling that implementing green spaces within the focus area produced, the maximum negative ΔT_{2m} value in each bin was obtained for each greening strategy and at each time step.

Since this method just looks for the maximum value within the downwind domain, it can be susceptible to the small scale noise that can skew ΔT_{2m} values and be more reflective of stochastic turbulence and not just the effect of land use conversion. However, after examining all of the individual time steps, the method does seem to provide a good estimate of the advective cooling, especially after averaging over a longer time frame. Because of this, the mean maximum downwind

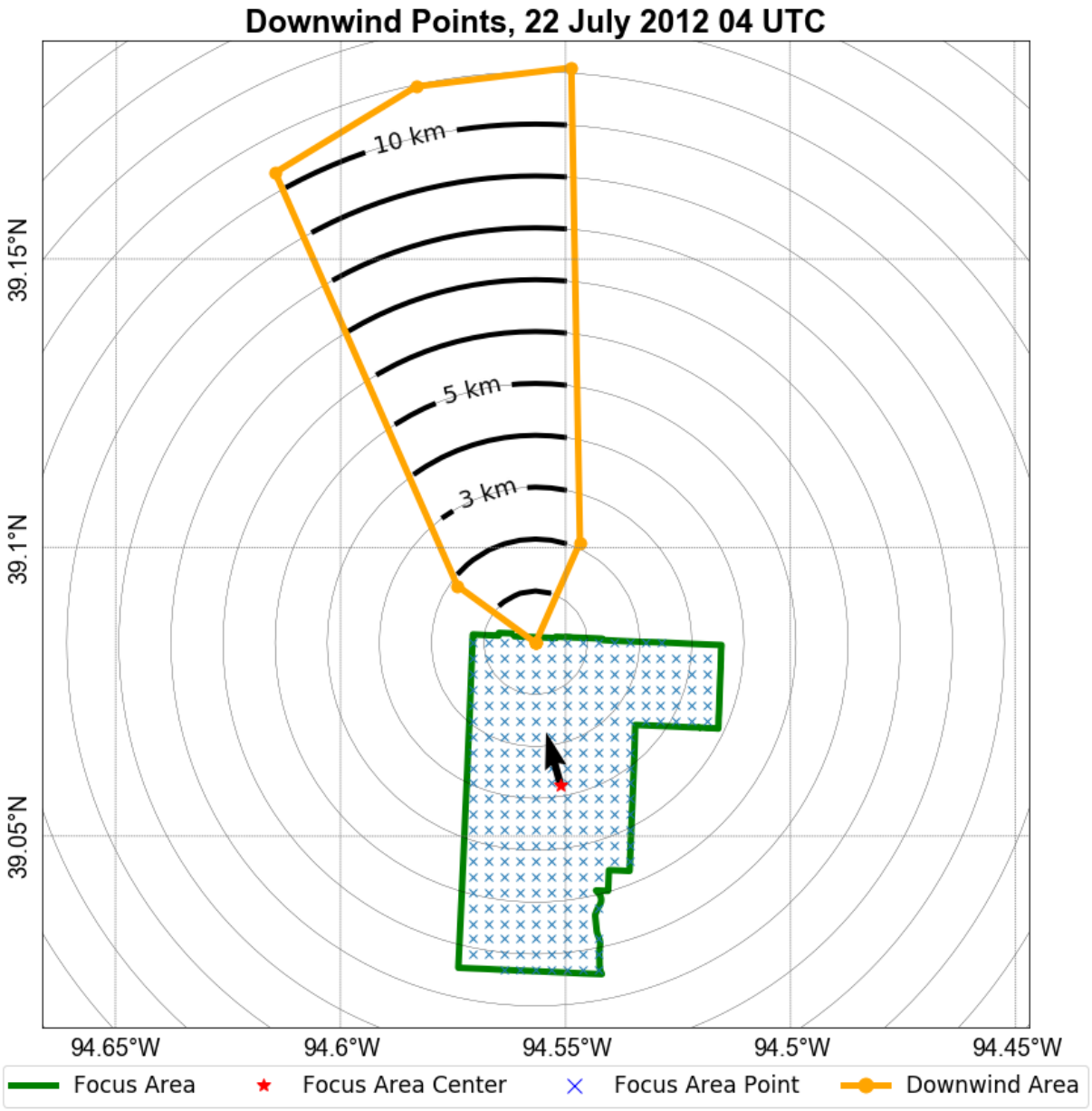

Figure 3.9: Example of the process used to determine grid points downwind of the focus area, with the focus area (green) and downwind area (orange) outlined. The central focus area grid point (red star) and other focus area points (blue 'X') are marked. 1-km distance rings relative to the edge point are contoured (gray).

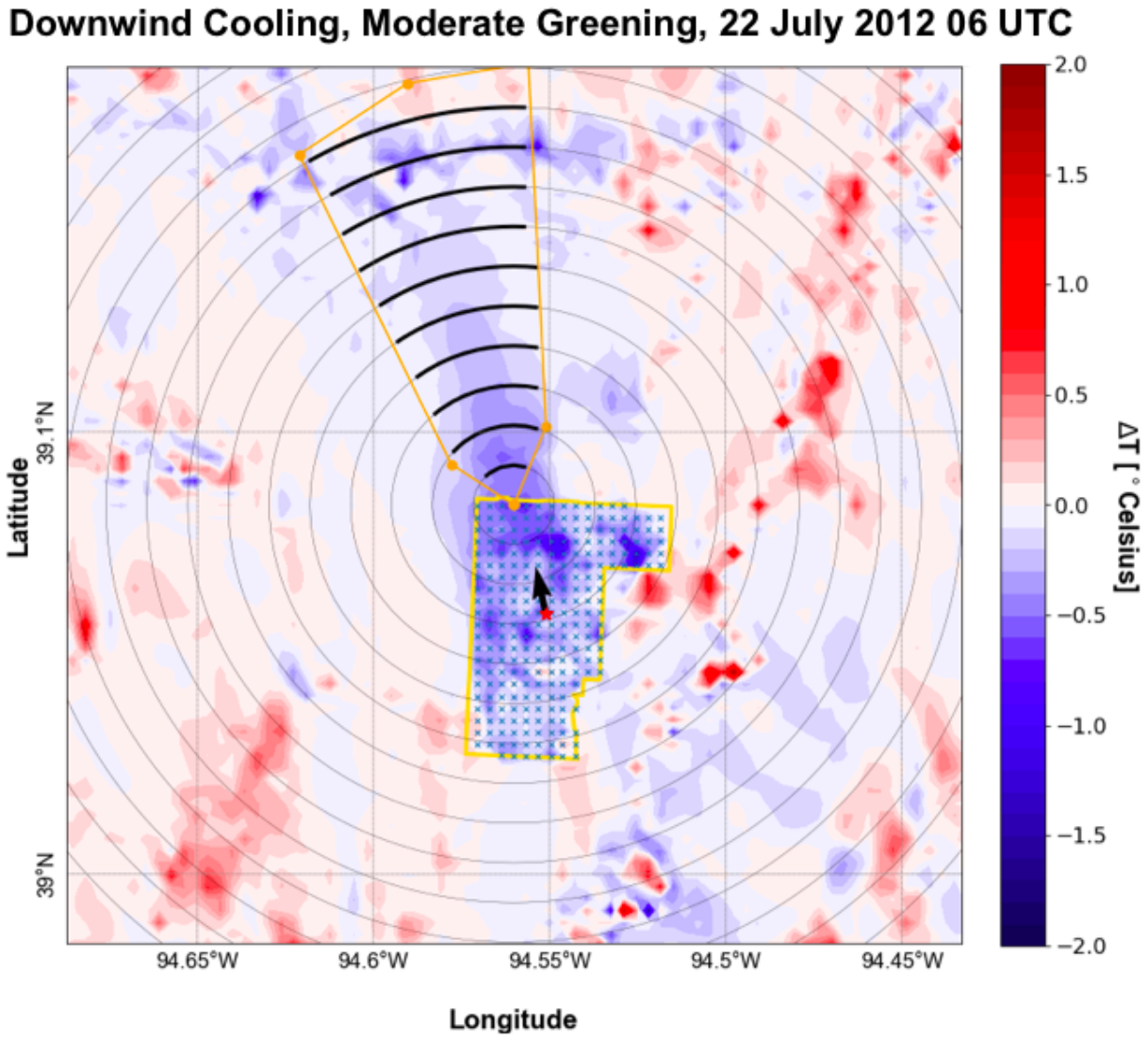

Figure 3.10: Downwind cooling signal observed in the ΔT_{2m} (°C) under moderate greening at 06 UTC 22 July 2012 (Case 1), utilizing the method depicted in Figure 3.9.

cooling was assessed across all three experimental cases. ΔT_{2m} values were separated across four 6-hour periods of the diurnal cycle: 14 – 19 UTC (early day), 20 – 01 UTC (late day), 02 – 07 UTC (early night) and 08 – 13 (late night). The results of this analysis are visualized in Figure 3.11.

Overall, the advection of cooler air from the focus area to downwind areas produced a weak but noticeable negative ΔT_{2m} signal. This signal was confined mostly to locations within 0.2 – 1 km of the focus area boundary. The downwind cooling impact beyond 1.5 km from the focus area was found to be negligible across all time periods and extents of greening, and is thus not shown. Similar to the results obtained in analyzing the local cooling effects of urban greening, the magnitude of downwind cooling exhibited variation with both the diurnal cycle and the greening extent. Downwind cooling was greatest during the early night period (02 – 07 UTC), with median maximum downwind cooling values for the aggressive greening simulations reaching over 1.0°C 1km downwind of the boundary of the focus area. This time period aligns with the peak of the local cooling effects analyzed in Section 4.3, making the stronger advection seen here unsurprising due to the stronger local temperature gradient present across the area. Unlike what was observed in the local cooling analysis, however, a similarly strong signal was present in the late day (20 – 01 UTC) period. This can be attributed to the presence of a stronger surface wind and well-mixed daytime boundary layer, which increases potential cold air advection to downwind locations.

Median and 75th percentile values of maximum downwind cooling up to 1.6 km from the focus area are listed for each of the defined time periods in Tables 3.4, 3.5, 3.6, and 3.7. Similar to what was determined in the analysis of local cooling, downwind reductions of ΔT_{2m} associated with the conservative greening strategy were weak compared to the results of the more extensive simulations. Conversely, the moderate and aggressive strategies were found to reduce nocturnal urban temperatures by up of 1.0 to 1.25 °C out to 1 km downwind of the focus area.

Interestingly, the largest downwind cooling impacts were consistently found 1 km away from the focus area across all simulations and greening strategies, and minimum ΔT_{2m} values were found to decrease linearly at distances approaching this value before sharply increasing. This may be due to the systematic influence of model-generated turbulence or convection. However, Dimoudi &

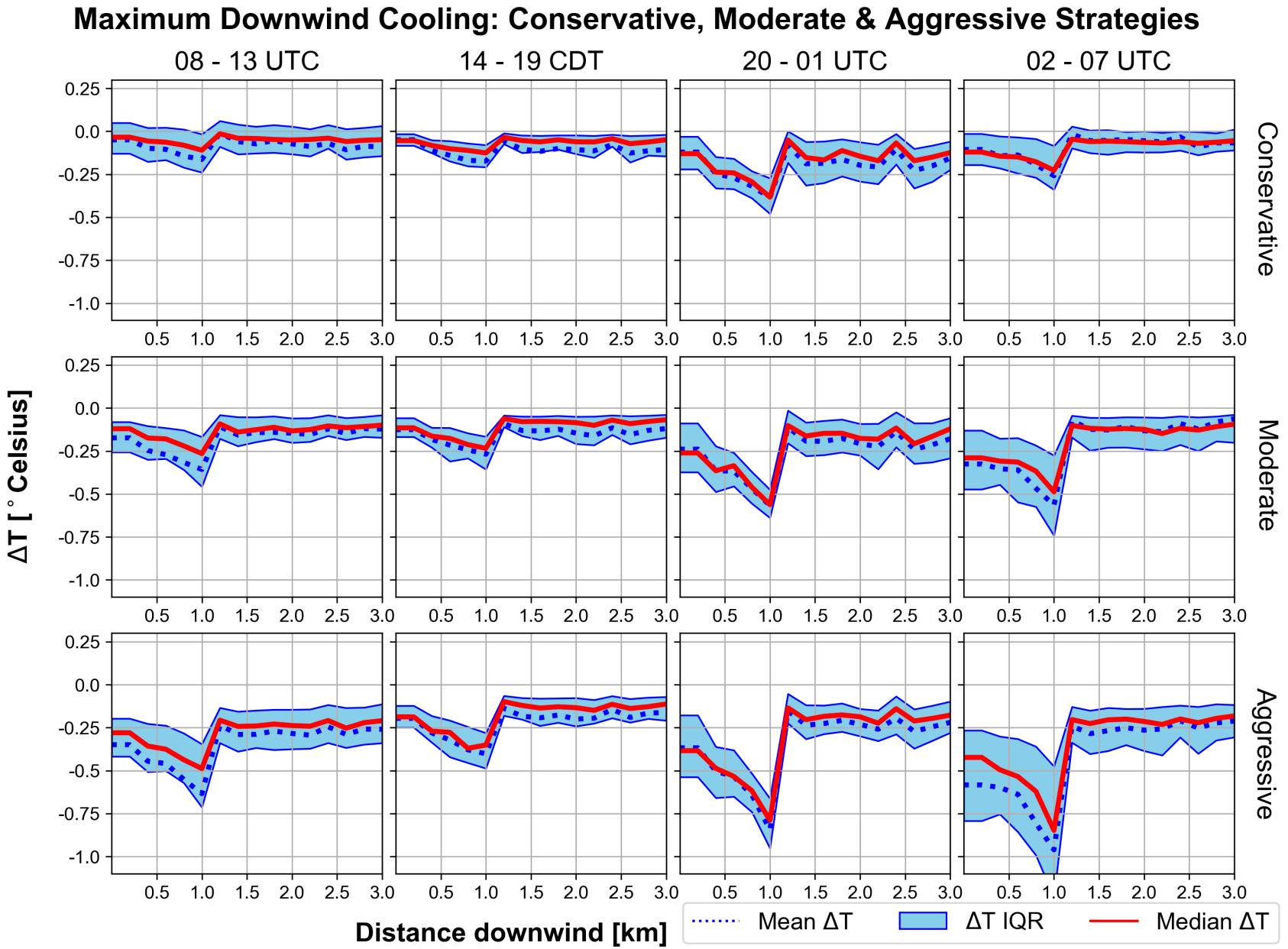

Figure 3.11: Analysis of maximum cooling downwind from the focus area for the three simulations combined and each greening strategy, consisting of the mean maximum negative ΔT_{2m} value at 200-meter increments downwind from the edge of the focus area across four defined time periods. Shown for each strategy and time period are the mean (red), median (blue) and interquartile range (blue shaded) of the obtained maximum negative ΔT_{2m} values.

Nikolopoulou 2003 notes a similar cooling effect downwind of a simulated urban green space, albeit at a smaller scale attributed to the influences of terrain and local urban morphology.

While the results presented here are promising in demonstrating the benefits of urban greening, they also show that UHI reduction in the Kansas City area is likely to necessitate a more comprehensive urban greening plan should land use conversion be adopted as a mitigation technique. In terms of similar studies regarding the extension of the "park cool island" into surrounding areas, both the extent and magnitude of downwind cooling observed in these simulations is in line previous observational studies such as Doick *et al.* 2014 and Feyisa *et al.* 2014 as well as modeling studies such as Declet-Barreto *et al.* 2013. Nonetheless, additional model simulations encompassing a greater variety of UHI mitigation strategies and synoptic weather patterns are necessary to investigate the matter further.

Table 3.4: Median (Q50) and 75th percentile (Q75) maximum downwind cooling (°C) for all three cases combined, calculated at 0.2-kilometer increments (DX) downwind from the boundary of the focus area at each time step. Results are restricted to the 08 – 13 UTC period and are separated by greening scenario.

Maximum Downwind Cooling: 08 – 13 UTC

	Conservative		**Moderate**		**Aggressive**	
DX (km)	**Q50**	**Q75**	**Q50**	**Q75**	**Q50**	**Q75**
0.2	-0.03	-0.13	-0.12	-0.26	-0.28	-0.42
0.4	-0.06	-0.18	-0.17	-0.30	-0.36	-0.51
0.6	-0.06	-0.17	-0.18	-0.30	-0.37	-0.50
0.8	-0.08	-0.21	-0.22	-0.36	-0.44	-0.57
1.0	-0.11	-0.24	-0.26	-0.46	-0.49	-0.71
1.2	-0.01	-0.09	-0.09	-0.18	-0.21	-0.34
1.4	-0.04	-0.13	-0.14	-0.22	-0.24	-0.39
1.6	-0.04	-0.13	-0.13	-0.20	-0.24	-0.37

Table 3.5: As in Table 3.4, but for the 14 – 19 UTC period.

Maximum Downwind Cooling: 14 – 19 UTC

	Conservative		**Moderate**		**Aggressive**	
DX (km)	**Q50**	**Q75**	**Q50**	**Q75**	**Q50**	**Q75**
0.2	-0.05	-0.08	-0.11	-0.17	-0.19	-0.25
0.4	-0.08	-0.12	-0.16	-0.23	-0.27	-0.34
0.6	-0.10	-0.17	-0.18	-0.31	-0.28	-0.42
0.8	-0.11	-0.20	-0.21	-0.29	-0.37	-0.45
1.0	-0.12	-0.20	-0.23	-0.36	-0.35	-0.49
1.2	-0.04	-0.07	-0.06	-0.11	-0.09	-0.18
1.4	-0.06	-0.13	-0.08	-0.16	-0.12	-0.20
1.6	-0.06	-0.12	-0.08	-0.19	-0.13	-0.24

Table 3.6: As in Table 3.4, but for the 20 – 01 UTC period.

Maximum Downwind Cooling: 20 – 01 UTC

	Conservative		Moderate		Aggressive	
DX (km)	**Q50**	**Q75**	**Q50**	**Q75**	**Q50**	**Q75**
0.2	-0.13	-0.22	-0.26	-0.37	-0.38	-0.54
0.4	-0.23	-0.33	-0.36	-0.49	-0.49	-0.66
0.6	-0.24	-0.34	-0.34	-0.46	-0.53	-0.65
0.8	-0.29	-0.39	-0.46	-0.56	-0.62	-0.74
1.0	-0.38	-0.47	-0.56	-0.64	-0.79	-0.95
1.2	-0.05	-0.18	-0.10	-0.20	-0.13	-0.22
1.4	-0.15	-0.31	-0.16	-0.28	-0.20	-0.32
1.6	-0.16	-0.30	-0.14	-0.27	-0.18	-0.29

Table 3.7: As in Table 3.4, but for the 02 – 07 UTC period.

Maximum Downwind Cooling: 02 – 07 UTC

	Conservative		Moderate		Aggressive	
DX (km)	**Q50**	**Q75**	**Q50**	**Q75**	**Q50**	**Q75**
0.2	-0.12	-0.20	-0.29	-0.47	-0.42	-0.79
0.4	-0.14	-0.22	-0.31	-0.45	-0.49	-0.75
0.6	-0.15	-0.24	-0.31	-0.55	-0.53	-0.86
0.8	-0.17	-0.27	-0.37	-0.57	-0.62	-1.00
1.0	-0.23	-0.34	-0.49	-0.74	-0.85	-1.24
1.2	-0.04	-0.09	-0.10	-0.17	-0.20	-0.33
1.4	-0.06	-0.13	-0.12	-0.25	-0.23	-0.40
1.6	-0.06	-0.14	-0.12	-0.23	-0.20	-0.38

Chapter 4

Discussion and Conclusions

4.1 Summary

Elevated near-surface air temperatures due to the urban heat island (UHI) pose an increasingly dire threat to residents of the world's cities, with impacts expected to increase in the coming decades due to the combined forces of urbanization and anthropogenic global warming (Revi *et al.* 2014; Field 2017; Frumkin 2002). Recently, efforts have been made to counteract the UHI by implementing green spaces (e.g. parks, urban forests, cropland) into urbanized areas to increase surface latent heat flux and thereby reduce the air temperature (Schilling & Logan 2008; Hart & Sailor 2009; Oliveira *et al.* 2011). While the potential effects of urban greening are difficult to quantify at large scales, the use of numerical weather simulations to analyze the thermal impacts of land use conversion offer a useful avenue by which greenspace implementation can be assessed (Santamouris 2013; Papangelis *et al.* 2012; Zhou & Shepherd 2010). Thus, this study sought to bridge atmospheric modeling and urban planning by investigating the potential for urban greening to provide UHI abatement in economically underserved portions of the Kansas City metropolitan area through the use of high-resolution numerical weather simulations.

In accordance with recent urban greening efforts (e.g., Colasanti *et al.* 2012; Meerow & Newell 2017), a portion of the Kansas City area with high vacancy rates was first identified as a potential location where large-scale green space implementation would be potentially feasible (Figure 2.2). To examine the possible impacts of urban greening within this "focus area", the Weather Research and Forecasting (WRF) model (Skamarock *et al.* 2005) was utilized to simulate the response of the Kansas City UHI to large-scale changes in land use characteristics. A triple-nested model grid

was implemented in WRF (Figure 2.3) with a maximum horizontal resolution of 0.3 km and 96 vertical levels (Figure 2.4) to capture a block-level near-surface air temperature field as well as impacts of the UHI to the structure of planetary boundary layer. Furthermore, high-resolution land use/land cover data from the National Land Cover Database (NLCD) was ingested into the model system and interpolated to the model domain to represent fine scale variations in land surface characteristics across the heterogeneous urban landscape within the focus area.

Due to WRF's many microphysical and boundary layer parameterization options, a series of sensitivity tests was first performed to determine the best model configuration to use in simulating the effects of implemented green spaces. In examining the model's performance in replicating summertime 2-meter air temperatures within urbanized (Figure 2.6) and non-urbanized (Figure 2.7) locations, it was determined that the Single Layer Urban Canopy Model (SLUCM) and Bougeault–Lacarrere boundary layer scheme performed strongest (Table 2.2). Following this, three potential urban greening scenarios of increasing extent were determined for use in experimental simulations based on local residential vacancy rates within the focus area. The land use/land cover data within the model system was subsequently modified to reflect these potential scenarios (Table 2.4). Finally, experimental WRF runs encompassing three five-day periods of elevated summertime heat were performed for each greening scenario along with a control run with no modifications made to the land use/land cover data (Table 2.3).

Using results from the experimental WRF simulations, three major aspects were assessed. Initially, to provide a baseline examination of how the model system resolved the Kansas City UHI, its structure and diurnal evolution were analyzed for each of the three control simulations. In accordance with previous observational and modeling studies, a positive linear relationship between the urban fraction at each grid cell within the innermost model domain and the simulated 2-meter air temperature (T_{2m}) was identified (Figure 3.3). This relationship was more pronounced during the nighttime (12 – 02 UTC) hours following the development of the stable nocturnal boundary layer. A diurnal analysis of T_{2m} at the previously utilized urban and non-urban sites further demonstrated WRF's resolution of the Kansas City UHI, with urban heat island intensity (UHII) shown to reach

up to 5 °C during the overnight hours (Figure 3.4). Finally, T_{2m} was assessed across the dominant NLCD land use classifications used within the model system, showing an increasing relationship between urban density and temperature that was also more pronounced at night (Figure 3.5).

The primary objective of the analysis was to examine the cooling impact of the implemented green spaces in each experimental simulation. In doing so, the ΔT_{2m} dataset was created by simply calculating the difference in T_{2m} between the experimental and control simulations of each of the three cases. This allowed for the impacts of urban greening across the diurnal cycle for varying degrees of urban greening to be quantified (Figure 3.7) and for the statistical significance of greenspace-induced cooling to be calculated (Tables 3.1, 3.2, and 3.3). Overall, the outcome of the Conservative greening simulations showed minimal statistically significant UHI abatement within the focus area. However, results from the Moderate and Aggressive greening scenarios indicate that more extensive urban greenspace implementation has the potential to reduce median nocturnal temperatures within the focus area by 0.5 to 1.0 °C during the overnight hours. These results were shown to exhibit widespread significance at or below the $p = 0.001$ level. As observed in past observational studies within urban landscapes, the cooling impacts resolved by the model system were attributable to heightened latent heat flux and lowered sensible heat flux stemming from the implementation of urban green spaces (Figure 3.8).

Given the previously identified extension of the "park cool island" into surrounding non-vegetated areas via cold air advection, the potential downwind cooling impacts of urban greening within the focus area was also analyzed. To do so, points downwind of the boundary of the focus area were determined via the synoptic wind direction at its center (Figures 3.9 and 3.10) at each time step. Next, the minimum downwind value of ΔT_{2m} (i.e. the maximum cooling amount) at 0.2 km increments from the boundary was determined. Results from this analysis (Figure 3.11 and Tables 3.4 – 3.7) further indicate that the Conservative greening strategy resulted in minimal reduction to local UHI impacts. However, the results of the Moderate and Aggressive greening simulations were shown to provide a downwind cooling impact of up to 1.0 °C at locations up to 1 km downwind of the focus area.

4.2 Conclusions

Ultimately, the results shown here support the development of strategies to convert abandoned buildings and unused impervious surfaces into urban green spaces as part of a greater effort to reduce the negative ramifications of the UHI. These results must be put into a multidisciplinary context. From an atmospheric modeling perspective, this study demonstrates the ability of high-resolution numerical weather models such as WRF to resolve the UHI and its response to changes in land cover at approximately block-level. Similar experiments have been conducted in studies such as Zhou & Shepherd 2010; Papangelis *et al.* 2012; Morini *et al.* 2016, and Fu & Weng 2017. While past work has been strong in demonstrating the applicability of numerical modeling to simulations examining UHI abatement, these previous depictions of urban greening have generally not been feasible for urban planning applications (e.g. the use of green roofs across an entire city or the conversion large industrial areas to vegetated green spaces). Here, we present simulations of urban greening that are both feasible in nature and targeted within a region which could achieve greater physical, cultural, and economic health upon implementation.

Despite the more feasible nature in which urban greening has been implemented in this study, its limitations must still be considered. As seen in the analyses of both the local and downwind effects of greening, obtaining significant cooling was confined to the Moderate and Aggressive strategies and the majority of significant cooling impacts had a magnitude of 1.0 °C or below. Within the model system, it is difficult to determine the key inhibitors to greenspace-induced cooling using only three case studies at a single location under similar synoptic weather patterns. Explanations may include the advection of warmer upwind air into the focus area or the influence of mixing in the lower PBL. Regardless, additional case studies under a greater variety of locations and synoptic settings are required to further examine the physical factors which may limit the cooling impacts of urban green spaces. This study is further limited due to the inadequacy of numerical models such as WRF to directly resolve both sub-grid scale physical processes (e.g. boundary layer turbulence) and fully account for heterogeneous urban morphology. While the nested grid setup, high inner domain resolution, advanced parameterization schemes, and a fractional land use grid were

utilized to account for this, a more in depth analysis of urban greening within the focus area may potentially be achieved using a computational fluid dynamics (CFD) model simulation. However, given the results of the control case, the WRF is able to realistically capture the UHI.

While the reduction of 2-meter air temperature by 0.5 to 1.0 °C is unlikely to eliminate heat-related illnesses or mortality during summertime heat waves, these results present more realistic numbers for planners to consider when exploring potential avenues for UHI mitigation. Of course, the large-scale conversion of vacant land at a level reflecting the Moderate or Aggressive greening strategies of this study is still both financially and temporally expensive. However, the potential benefits of both reducing the UHI and also driving reinvestment in a community's natural environment make it a useful option to explore in areas with high land use conversion potential such as the focus area of this study. While UHI mitigation might be a secondary reason for land use conversion, it at least provides an additional incentive. It is hoped that this and other future work in this area can be used as a guidance tool to promote the usefulness of urban greening to reduce the impacts of the UHI and ultimately promote sustainable future cities.

References

1. Akbari, H. *et al.* Local climate change and urban heat island mitigation techniques–the state of the art. *Journal of Civil Engineering and Management* **22,** 1–16 (2016).

2. Arnfield, A. J. Two decades of urban climate research: a review of turbulence, exchanges of energy and water, and the urban heat island. *International Journal of Climatology* **23,** 1–26 (2003).

3. Azevedo, J. A., Chapman, L. & Muller, C. L. Quantifying the daytime and night-time urban heat island in Birmingham, UK: A comparison of satellite derived land surface temperature and high resolution air temperature observations. *Remote Sensing* **8,** 153 (2016).

4. Banks, R. F. *et al.* Sensitivity of boundary-layer variables to PBL schemes in the WRF model based on surface meteorological observations, lidar, and radiosondes during the HygrA-CD campaign. *Atmospheric Research* **176,** 185–201 (2016).

5. Barlow, J. F., Halios, C. H., Lane, S. & Wood, C. R. Observations of urban boundary layer structure during a strong urban heat island event. *Environmental Fluid Mechanics* **15,** 373–398 (2015).

6. Bohnenstengel, S., Evans, S, Clark, P. A. & Belcher, S. Simulations of the London urban heat island. *Quarterly Journal of the Royal Meteorological Society* **137,** 1625–1640 (2011).

7. Borden, K. A. & Cutter, S. L. Spatial patterns of natural hazards mortality in the United States. *International journal of health geographics* **7,** 64 (2008).

8. Bougeault, P. & Lacarrere, P. Parameterization of orography-induced turbulence in a mesobeta–scale model. *Monthly Weather Review* **117,** 1872–1890 (1989).

9. Chen, F. *et al.* The integrated WRF/urban modelling system: development, evaluation, and applications to urban environmental problems. *International Journal of Climatology* **31,** 273–288 (2011).

10. Childs, P. P. & Raman, S. Observations and numerical simulations of urban heat island and sea breeze circulations over New York City. *Pure and Applied Geophysics* **162,** 1955–1980 (2005).

11. Chow, W. T., Pope, R. L., Martin, C. A. & Brazel, A. J. Observing and modeling the nocturnal park cool island of an arid city: horizontal and vertical impacts. *Theoretical and Applied Climatology* **103,** 197–211 (2011).

12. City of Kansas City, Division of Community Engagement, Policy and Accountability. A Segregated Kansas City is Not Good For Our Health. *KCMO Public Health Connection* **37,** 1–6 (2017).

13. Colasanti, K. J., Hamm, M. W. & Litjens, C. M. The city as an" agricultural powerhouse"? perspectives on expanding urban agriculture from Detroit, Michigan. *Urban Geography* **33,** 348–369 (2012).

14. Danielson, J. J. & Gesch, D. B. *Global multi-resolution terrain elevation data 2010 (GMTED2010)* tech. rep. (U.S. Geological Survey, 2011).

15. Declet-Barreto, J., Brazel, A. J., Martin, C. A., Chow, W. T. & Harlan, S. L. Creating the park cool island in an inner-city neighborhood: heat mitigation strategy for Phoenix, AZ. *Urban Ecosystems* **16,** 617–635 (2013).

16. Dimoudi, A. & Nikolopoulou, M. Vegetation in the urban environment: microclimatic analysis and benefits. *Energy and buildings* **35,** 69–76 (2003).

17. Dixon, P *et al.* Association of weekly suicide rates with temperature anomalies in two different climate types. *International journal of environmental research and public health* **11,** 11627–11644 (2014).

18. Doick, K. J., Peace, A. & Hutchings, T. R. The role of one large greenspace in mitigating London's nocturnal urban heat island. *Science of the total environment* **493,** 662–671 (2014).

19. Estoque R. C., M. Y.M.S. W. Effects of landscape composition and pattern on land surface temperature: An urban heat island study in the megacities of Southeast Asia. *Science of the Total Environment* **577,** 349–359 (2017).

20. Feyisa, G. L., Dons, K. & Meilby, H. Efficiency of parks in mitigating urban heat island effect: An example from Addis Ababa. *Landscape and Urban Planning* **123,** 87–95 (2014).

21. Field, C. B. *Climate change 2014–Impacts, adaptation and vulnerability: Regional aspects* (Cambridge University Press, 2017).

22. Fouillet, A. *et al.* Excess mortality related to the August 2003 heat wave in France. *International archives of occupational and environmental health* **80,** 16–24 (2006).

23. Frumkin, H. Urban sprawl and public health. *Public Health Reports* **117,** 201–217 (2002).

24. Fu, P. & Weng, Q. Responses of urban heat island in Atlanta to different land-use scenarios. *Theoretical and Applied Climatology,* 1–13 (2017).

25. Giannaros, C., Nenes, A., Giannaros, T. M., Kourtidis, K. & Melas, D. A comprehensive approach for the simulation of the Urban Heat Island effect with the WRF/SLUCM modeling system: The case of Athens (Greece). *Atmospheric Research* **201,** 86–101 (2018).

26. Glotfelty, T. *et al.* NUDAPT 44 Documentation (2013).

27. Gutiérrez, E., González, J. E., Martilli, A., Bornstein, R. & Arend, M. Simulations of a heat-wave event in New York City using a multilayer urban parameterization. *Journal of Applied Meteorology and Climatology* **54,** 283–301 (2015).

28. Halios, C. H. & Barlow, J. F. Observations of the morning development of the urban boundary layer over London, UK, taken during the ACTUAL project. *Boundary-layer meteorology* **166,** 395–422 (2018).

29. Hardin, A., Liu, Y, Cao, G & Vanos, J. Urban heat island intensity and spatial variability by synoptic weather type in the northeast US. *Urban Climate* (2017).

30. Hart, M. A. & Sailor, D. J. Quantifying the influence of land-use and surface characteristics on spatial variability in the urban heat island. *Theoretical and applied climatology* **95,** 397–406 (2009).

31. Heckert, M. & Mennis, J. The economic impact of greening urban vacant land: a spatial difference-in-differences analysis. *Environment and Planning A* **44,** 3010–3027 (2012).

32. Homer, C. *et al.* Completion of the 2011 National Land Cover Database for the conterminous United States–representing a decade of land cover change information. *Photogrammetric Engineering & Remote Sensing* **81,** 345–354 (2015).

33. Hong, S.-Y., Noh, Y. & Dudhia, J. A new vertical diffusion package with an explicit treatment of entrainment processes. *Monthly weather review* **134,** 2318–2341 (2006).

34. Hong, S.-Y., Dudhia, J. & Chen, S.-H. A revised approach to ice microphysical processes for the bulk parameterization of clouds and precipitation. *Monthly Weather Review* **132,** 103–120 (2004).

35. Hu, L. & Brunsell, N. A. A new perspective to assess the urban heat island through remotely sensed atmospheric profiles. *Remote Sensing of Environment* **158,** 393–406 (2015).

36. Iacono, M. J. *et al.* Radiative forcing by long-lived greenhouse gases: Calculations with the AER radiative transfer models. *Journal of Geophysical Research: Atmospheres* **113** (2008).

37. Imhoff, M. L., Zhang, P., Wolfe, R. E. & Bounoua, L. Remote sensing of the urban heat island effect across biomes in the continental USA. *Remote Sensing of Environment* **114,** 504–513 (2010).

38. Janjić, Z. I. The step-mountain eta coordinate model: Further developments of the convection, viscous sublayer, and turbulence closure schemes. *Monthly Weather Review* **122,** 927–945 (1994).

39. Johnson, D. P. & Wilson, J. S. The socio-spatial dynamics of extreme urban heat events: The case of heat-related deaths in Philadelphia. *Applied Geography* **29,** 419–434 (2009).

40. Jones, T. S. *et al.* Morbidity and Mortality Associated With the July 1980 Heat Wave in St Louis and Kansas City, Mo. *Journal of the American Medical Association* **247,** 3327–3331 (1982).

41. Kain, J. S. The Kain–Fritsch convective parameterization: an update. *Journal of Applied Meteorology* **43,** 170–181 (2004).

42. Kusaka, H., Kondo, H., Kikegawa, Y. & Kimura, F. A simple single-layer urban canopy model for atmospheric models: Comparison with multi-layer and slab models. *Boundary-Layer Meteorology* **101,** 329–358 (2001).

43. Li, D. & Bou-Zeid, E. Quality and sensitivity of high-resolution numerical simulation of urban heat islands. *Environmental Research Letters* **9,** 055001 (2014).

44. Li, D. & Bou-Zeid, E. Synergistic interactions between urban heat islands and heat waves: The impact in cities is larger than the sum of its parts. *Journal of Applied Meteorology and Climatology* **52,** 2051–2064 (2013).

45. Li, H., Wolter, M., Wang, X. & Sodoudi, S. Impact of land cover data on the simulation of urban heat island for Berlin using WRF coupled with bulk approach of Noah-LSM. *Theoretical and applied climatology,* 1–15 (2017).

46. Li, J. *et al.* Impacts of landscape structure on surface urban heat islands: A case study of Shanghai, China. *Remote Sensing of Environment* **115,** 3249–3263 (2011).

47. Li, X.-X. & Norford, L. K. Evaluation of cool roof and vegetations in mitigating urban heat island in a tropical city, Singapore. *Urban Climate* **16,** 59–74 (2016).

48. Liu, Y., Chen, F., Warner, T. & Basara, J. Verification of a mesoscale data-assimilation and forecasting system for the Oklahoma City area during the Joint Urban 2003 field project. *Journal of applied meteorology and climatology* **45,** 912–929 (2006).

49. L'Heureux, M.-A. The creative class, urban boosters, and race: shaping urban revitalization in Kansas City, Missouri. *Journal of Urban History* **41,** 245–260 (2015).

50. Mahrt, L. Nocturnal boundary-layer regimes. *Boundary-layer meteorology* **88,** 255–278 (1998).

51. Martilli, A., Clappier, A. & Rotach, M. W. An urban surface exchange parameterisation for mesoscale models. *Boundary-Layer Meteorology* **104,** 261–304 (2002).

52. Meehl, G. A. & Tebaldi, C. More intense, more frequent, and longer lasting heat waves in the 21st century. *Science* **305,** 994–997 (2004).

53. Meerow, S. & Newell, J. P. Spatial planning for multifunctional green infrastructure: Growing resilience in Detroit. *Landscape and Urban Planning* **159,** 62–75 (2017).

54. Memon, R. A., Leung, D. Y. & Liu, C.-H. An investigation of urban heat island intensity (UHII) as an indicator of urban heating. *Atmospheric Research* **94,** 491–500 (2009).

55. Mid-America Regional Council. *MARC Member Cities and Counties* Accessed = 2019-03-05. 2018. `http://marc.org/About-MARC/General-Information/Member-Cities-and-Counties`.

56. Mid-America Regional Council. *Troost Corridor Redevelopment Plan: A Plan for a Sustainable Troost Avenue* 2013.

57. Morini, E., Touchaei, A. G., Castellani, B., Rossi, F. & Cotana, F. The impact of albedo increase to mitigate the urban heat island in Terni (Italy) using the WRF model. *Sustainability* **8,** 999 (2016).

58. Murage, P., Hajat, S. & Kovats, R. S. Effect of night-time temperatures on cause and age-specific mortality in London. *Environmental Epidemiology* **1,** e005 (2017).

59. Nunez, M. & Oke, T. R. The energy balance of an urban canyon. *Journal of Applied Meteorology* **16,** 11–19 (1977).

60. Oke, T. The energetic basis of the urban heat island. *Quarterly Journal of the Royal Meteorological Society* **108,** 1–24 (1982).

61. Oke, T. in *Wind climate in cities* 81–107 (Springer, 1995).

62. Oke, T. The urban energy balance. *Progress in Physical Geography* **12,** 471–508 (1988).

63. Oliveira, S., Andrade, H. & Vaz, T. The cooling effect of green spaces as a contribution to the mitigation of urban heat: A case study in Lisbon. *Building and Environment* **46,** 2186–2194 (2011).

64. Pagano, M. A. & Bowman, A. O. *Vacant land in cities: An urban resource* (Brookings Institution, Center on Urban and Metropolitan Policy Washington, DC, 2000).

65. Papangelis, G., Tombrou, M., Dandou, A. & Kontos, T. An urban "green planning" approach utilizing the Weather Research and Forecasting (WRF) modeling system. A case study of Athens, Greece. *Landscape and urban planning* **105,** 174–183 (2012).

66. Peng, S. *et al.* Surface urban heat island across 419 global big cities. *Environmental science & technology* **46,** 696–703 (2011).

67. Revi, A., Satterthwaite, D. E., Aragón-Durand, F., Corfee-Motlot, J., *et al.* in *Climate Change 2014: Impacts, Adaptation, and Vulnerability. Part A: Global and Sectoral Aspects. Contribution of Working Group II to the Fifth Assessment Report of the Intergovernmental Panel on Climate Change* 535–612 (Cambridge University Press, Cambridge, 2014).

68. Robinson, P. J. On the definition of a heat wave. *Journal of applied Meteorology* **40,** 762–775 (2001).

69. Ryu, Y.-H. & Baik, J.-J. Quantitative analysis of factors contributing to urban heat island intensity. *Journal of Applied Meteorology and Climatology* **51,** 842–854 (2012).

70. Salamanca, F., Krpo, A., Martilli, A. & Clappier, A. A new building energy model coupled with an urban canopy parameterization for urban climate simulations—part I. formulation, verification, and sensitivity analysis of the model. *Theoretical and applied climatology* **99,** 331 (2010).

71. Salamanca, F., Martilli, A. & Yagüe, C. A numerical study of the Urban Heat Island over Madrid during the DESIREX (2008) campaign with WRF and an evaluation of simple mitigation strategies. *International Journal of Climatology* **32,** 2372–2386 (2012).

72. Salamanca, F., Georgescu, M., Mahalov, A, Moustaoui, M & Wang, M. Anthropogenic heating of the urban environment due to air conditioning. *Journal of Geophysical Research: Atmospheres* **119,** 5949–5965 (2014).

73. Santamouris, M. Using cool pavements as a mitigation strategy to fight urban heat island—A review of the actual developments. *Renewable and Sustainable Energy Reviews* **26,** 224–240 (2013).

74. Santamouris, M. Cooling the cities–a review of reflective and green roof mitigation technologies to fight heat island and improve comfort in urban environments. *Solar energy* **103,** 682–703 (2014).

75. Schilling, J. & Logan, J. Greening the rust belt: A green infrastructure model for right sizing America's shrinking cities. *Journal of the American Planning Association* **74,** 451–466 (2008).

76. Semenza, J. C. *et al.* Heat-related deaths during the July 1995 heat wave in Chicago. *New England journal of medicine* **335,** 84–90 (1996).

77. Seto, K. C., Dhakal, S., Bento, A., Betsill, M., *et al.* in *Climate Change 2014: Mitigation of Climate Change. Contribution of Working Group III to the Fifth Assessment Report of the Intergovernmental Panel on Climate Change* 923–1000 (Cambridge University Press, Cambridge, 2014).

78. Shahmohamadi, P, Che-Ani, A., Maulud, K., Tawil, N. & Abdullah, N. The impact of anthropogenic heat on formation of urban heat island and energy consumption balance. *Urban Studies Research* **2011** (2011).

79. Skamarock, W. C. *et al. A description of the advanced research WRF version 2* tech. rep. (National Center For Atmospheric Research Boulder Co Mesoscale and Microscale Meteorology Div, 2005).

80. Susca, T., Gaffin, S. R. & Dell'Osso, G. Positive effects of vegetation: Urban heat island and green roofs. *Environmental pollution* **159,** 2119–2126 (2011).

81. Taha, H. Urban climates and heat islands: albedo, evapotranspiration, and anthropogenic heat. *Energy and buildings* **25,** 99–103 (1997).

82. Takebayashi, H. & Moriyama, M. Surface heat budget on green roof and high reflection roof for mitigation of urban heat island. *Building and Environment* **42,** 2971–2979 (2007).

83. Tan, J. *et al.* The urban heat island and its impact on heat waves and human health in Shanghai. *International journal of biometeorology* **54,** 75–84 (2010).

84. Tewari, M. *et al. Implementation and verification of the unified NOAH land surface model in the WRF model* in *20th conference on weather analysis and forecasting/16th conference on numerical weather prediction* **1115** (2004).

85. Tran, H., Uchihama, D., Ochi, S. & Yasuoka, Y. Assessment with satellite data of the urban heat island effects in Asian mega cities. *International Journal of Applied Earth Observation and Geoinformation* **8,** 34–48 (2006).

86. United Nations. *World Urbanization Prospects: The 2014 Revision, (ST/ESA/SER.A/366)* (United Nations, Department of Economic and Social Affairs, Population Division, 2015).

87. United States Census Bureau. *Annual Estimates of the Resident Population: April 1, 2010 to July 1, 2017, United States Metropolitan Statistical Area; and for Puerto Rico, 2017 Population Estimates* 2018.

88. United States Census Bureau. *Population Change for Metropolitan and Micropolitan Statistical Areas in the United States and Puerto Rico: 2000 to 2010 (CPH-T-2)* tech. rep. (United States Department of Commerce, 2011).

89. Voogt, J. *How researchers measure urban heat islands* in *United States Environmental Protection Agency (EPA), State and Local Climate and Energy Program, Heat Island Effect, Urban Heat Island Webcasts and Conference Calls* (2007).

90. Voogt, J. A. & Oke, T. R. Thermal remote sensing of urban climates. *Remote sensing of environment* **86,** 370–384 (2003).

91. Yuan, F. & Bauer, M. E. Comparison of impervious surface area and normalized difference vegetation index as indicators of surface urban heat island effects in Landsat imagery. *Remote Sensing of environment* **106,** 375–386 (2007).

92. Zhao, L. *et al.* Interactions between urban heat islands and heat waves. *Environmental Research Letters* **13,** 034003 (2018).

93. Zhou, Y. & Shepherd, J. M. Atlanta's urban heat island under extreme heat conditions and potential mitigation strategies. *Natural Hazards* **52,** 639–668 (2010).

Appendix A

NLCD Land Surface Parameters

Table A.1: Overview of land surface characteristics for each NLCD land use classification used within the study. Parameters include [1] Surface albedo (%), [2] Soil moisture availability (%), [3] Surface emissivity (%), [4] Roughness length (cm), and [5] Thermal inertia (0.01 cal cm^{-2} K^{-1} $s^{-0.5}$)

#	Category Name	ALBD[1]	SLMO[2]	SFEM[3]	SFZ0[4]	THERIN[5]
14	Cropland/Natural Vegetation Mosaic	18.0	0.25	0.985	30.0	4.0
21	Open Water	8.0	1.0	0.98	6.0	6.0
23	Developed, Open Space	12.0	0.10	0.97	30.0	3.0
24	Developed, Low Intensity	11.0	0.20	0.95	40.0	3.0
25	Developed, Medium Intensity	11.0	0.15	0.90	60.0	3.0
26	Developed, High Intensity	10.0	0.10	0.88	100.0	3.0
27	Barren Land (Rock/Sand/Clay)	20.0	0.02	0.90	5.0	2.0
28	Deciduous Forest	15.0	0.3	0.93	100.0	4.0
29	Evergreen Forest	12.0	0.3	0.95	100.0	4.0
30	Mixed Forest	13.0	0.3	0.97	100.0	4.0
32	Shrub/Scrub	20.0	0.1	0.93	15.0	3.0
33	Grassland/Herbaceous	19.0	0.15	0.96	7.0	3.0
37	Pasture/Hay	18.0	0.3	0.985	7.0	4.0
38	Cultivated Crops	18.0	0.5	0.985	10.0	4.0
39	Woody Wetlands	15.0	0.4	0.95	55.0	5.0
40	Emergent Herbaceous Wetlands	18.0	0.4	0.95	11.0	4.0